Powder Technology 416 (2023) 118209

Contents lists available at ScienceDirect

Powder Technology

journal homepage: www.journals.elsevier.com/powder-technology

Contact models for the multi-sphere discrete element method

Nathan Berry [a], Yonghao Zhang [b], Sina Haeri [a,*]

[a] School of Engineering, Institute for Materials and Processes, The University of Edinburgh, Edinburgh, Scotland, EH9 3FB, United Kingdom
[b] State Key Laboratory of High Temperature Gas Dynamics, Institute of Mechanics, Chinese Academy of Sciences, Beijing 100190, China

HIGHLIGHTS

- Five sources of error are found when implementing contact models for the MS-DEM.
- These errors are shown to be, in general, contact model independent.
- A new force summation procedure is established to prevent 3 error types.
- The definition of a local effect mass mitigates the remaining errors.
- All results are verified analytically and with simulations.

GRAPHICAL ABSTRACT

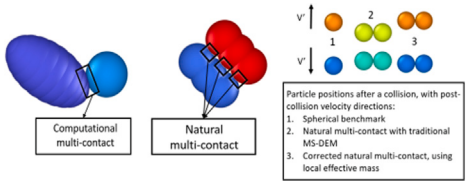

ARTICLE INFO

Keywords:
Non-spherical particles
Particle based methods
Multi-Sphere Discrete Element Method
DEM Clump
Glued Sphere DEM
Discrete Element Method
Contact models
MS-DEM contact models

ABSTRACT

Five sources of critical error are identified for binary interactions of particles using the Multi-Sphere Discrete Element Method (MS-DEM) i.e. the occurrence of under-damping, two forms of over-damping error, over-stiffness effects, and force response inconsistencies due to erroneous contact area calculations. Algorithmic issues are found to be the source of over-stiffness effects, one form of over-damping and the erroneous contact area calculations. The remaining over-damping and under-damping errors are physical in nature. By defining different types of MS-DEM interactions, solutions are proposed which can successfully mitigate all of the identified errors. This includes the development of the concept of a locally reduced mass to attenuate the physics-based form of over-damping, and purely algorithmic considerations rectify the other form of over-damping as well as the over-stiffness effects and erroneous contact area calculations. This study focuses on two types of linear spring dash-pot models and two non-linear Hertzian models, however, it is demonstrated the nature of the errors and their respective solutions are generally independent of the contact model. As such, the solutions proposed should be considered for implementation with other contact models when using the MS-DEM, with a high likelihood of being applicable to other contact detection methods.

1. Introduction

Particle morphology influences essentially all systems and processes that contain large numbers of solid particulates. This is evidenced by studies of bulk powder characteristics and flowability [1,2], particle segregation [3], spreadability in powder-based additive manufacturing processes [4,5], fluidised bed dynamics [6] and reactant quality [7]. The importance of understanding the effects of particle morphology on such systems, has motivated the development of numerous numerical methods to simulate aspherical particles, see [8–10] for reviews. The majority of the available methods are extensions of the Discrete Element Method (DEM), originally developed to model spherical particles [11]. The focus of this work is the popular extension of DEM known as the Multi-Sphere Discrete Element Method (MS-DEM) [12], which is a very common approach for simulating aspherical particles [9]. The MS-DEM – also known as the glued- or clumped-sphere or cluster DEM – rigidly fixes spherical DEM particles together to define a new particle, e.g. see Fig. 1. The MS-DEM has three advantages in comparison to other methods. Firstly, the algorithm used to detect

* Corresponding author.
E-mail address: s.haeri@ed.ac.uk (S. Haeri).

https://doi.org/10.1016/j.powtec.2022.118209
Received 5 November 2022; Received in revised form 26 December 2022; Accepted 28 December 2022
Available online 31 December 2022

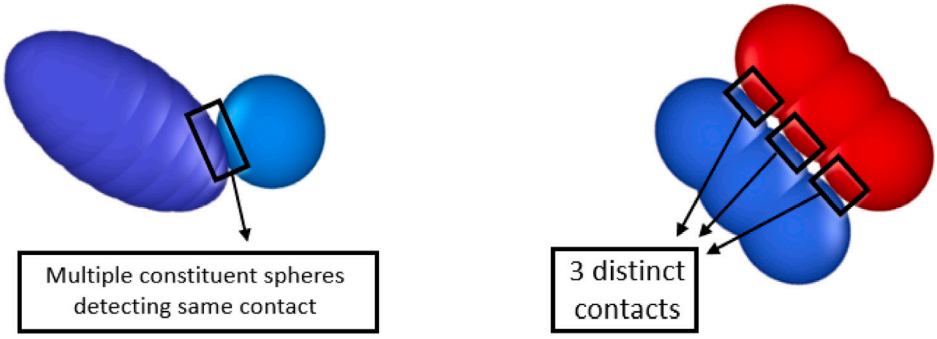

(a) Computational multi-contact point. (b) Natural multi-contact point.

Fig. 1. Types of MS-DEM multi-contact points.

particle contacts is the simplest of any other method for simulating non-spherical particles as it is identical to that for spheres. This minimises computational costs and allows for efficient handling of static friction forces that persist during the inter-particle contact [13]. Secondly, particles of almost arbitrary shape can be simulated unlike the majority of other techniques, which are analytically constrained. However, the MS-DEM is not suited to model sharp edges or extremely thin particles e.g. particles with high aspect ratios, for which spherocylinder methods may be more appropriate [14]. The third advantage commonly ascribed to the MS-DEM, is that reliable contact force models that have been developed and validated for spheres are assumed to be valid for the MS-DEM. This is in contrast to contact force models employed for other methods such as those used for simulating polyhedra and polygons whose accuracy is still open for debate [15].

The formulation and application of contact models for spheres, even before the considerations of particle morphology, is a complex endeavor. As contact models have to consider the underlying material properties of the particles, contact area and pre-collision velocities among other variables. Two of the most common classes of contact models used to handle the aforementioned variables in DEM simulations are linear spring dash-pot models and non-linear Hertzian models, which are the focus of this work and will be discussed extensively later in Section 3. Additionally, focus is given to the most common implementation of inter-particle friction for DEM simulations which is via a Coulomb stick and slip criteria. Interested readers are referred to the following non-exhaustive reviews for details of other models that are commonly used [16–18]. However, the important purported advantage of the MS-DEM that contact models developed and validated for spheres remain valid for the MS-DEM, has been previously questioned.

One of the earliest attempts to evaluate the validity of the MS-DEM was reported by Abbaspour-Fard [19], with the investigation of several MS-DEM collision scenarios. In that work, much of the focus is given to the concept of artificial roughness occurring in MS-DEM particle interactions. This effect occurs when uneven surfaces created from the particles' constituent spheres, cause unintended interlocking behaviour, resulting in an artificial increase in roughness/friction. Abbaspour-Fard then discussed how this phenomenon can be mitigated by improving the fidelity of the particle surfaces. Additionally, it was shown that additional damping occurred for collisions that contain multiple contact points while utilising velocity based damping, however, this was not highlighted as being erroneous behaviour. This concept of artificial roughness and the acknowledgement of multiple contact point collisions causing deviations in particle behaviour, has since been rigorously investigated.

Kruggel-Emden et al. [20], used the MS-DEM to generate spherical particles to perform collision tests with a flat wall, varying angle of impact, number of constituent spheres and their radii to construct the MS-DEM spheres. Deviations against data gathered from collisions using classical spherical DEM particles, could then be used to quantitatively evaluate the quality of a given MS-DEM interaction. One of the key conclusions from this work was that the artificial roughness could significantly impact the dynamics of a particle collision, particularly for its angular velocity response. Also highlighted in that work and the work of Price et al. [21], though no specific suggestions are given from the latter, is that contact models should be altered to ensure consistent MS-DEM particle behavior. Kruggel-Emden et al. [20] then suggested a simple approach to improve the consistency of an interaction containing multiple contact points, which is to divide the force occurring at a specific contact point by the total number of contact points. Interestingly, the authors offer little information as to why the contact forces should be modified, except for a brief note about unusual stiffness and damping behaviour that may occur. Later, Kodam et al. [22] pointed out that the simple solution posited by Kruggel-Emden et al. [20], division of forces with the number of contact points, will only hold for very specific cases, which will be discussed in detail in Section 9.

Using a similar simulation set-up to that of Kruggel-Emden et al. [20], with spherical particles constructed with the MS-DEM colliding with a wall, Kodam and co-workers [22] highlighted two errors that can be encountered when using the MS-DEM. Comparison of dynamics occurring from MS-DEM particle collision with that of a classical sphere, demonstrates that over-stiffness and over-damping effects can occur. Over-stiffness was identified as occurring when multiple constitutive spheres are simultaneously in contact (multi-contact point), over-damping was identified as occurring when velocity dependant damping is employed at a multi-contact point, both effects are to be discussed in great detail later. To solve the over-stiffness errors, Kodam et al. [22] suggested a procedure for adjusting multiple aspects of the given force model before simulations are carried out, by calibrating against the results of well defined interactions using a spherical benchmark. However, it is not clear how this calibration procedure could accurately be carried out for irregular particle interactions, which likely do not have predetermined well-defined interactions for comparison. Additionally, even the results from the well-defined spherical comparison are not consistent over the duration of a contact with respect to their benchmarks, however, an overall improvement from a ‘default’ MS-DEM procedure is achieved. No general solution for the over-damping effects were proposed, with Kodam et al. [22] suggesting that hysteric force models should be used to include damping in the MS-DEM, while recommending velocity based damping should be avoided. Additionally, in the work of Kodam et al. [22] tangential forces were not discussed.

In addition to the solutions proposed by Kruggel-Emden et al. [20] and Kodam et al. [22] to mitigate MS-DEM collision errors, Höhner et al. [23] have put forward an incremental technique to specifically address over-damping and over-stiffness errors. In this approach, the forces resulting from a multi-contact problem are advanced incrementally at each time step whilst being averaged over the number of contact points. Using a nearly identical set-up to Kruggel-Emden

Table 1
Previously identified errors and proposed solutions.

Error	Identified cause	Proposed solution(s)
Artificial roughness	Low fidelity particle representation.	To increase particle fidelity [19].
Over-stiffness	Occurrence of multiple contact points.	A priori adjustment of model parameters [22,24]. Adjust model parameters with number of contact points within a simulation [23,24].
Over-damping	Occurrence of multiple contact points with velocity based damping.	A priori adjustment of model parameters [24]. Adjust model parameters with number of contact points within a simulation [23,24], and avoid velocity based damping [22].

et al. [20] and Kodam et al. [22], the dynamics of a collision of spherical particle constructed using the MS-DEM are shown to be in excellent agreement with a spherical benchmark when this approach is implemented. Moreover, tangential forces are addressed in this method, unlike the proposals of Kodam et al. [22]. A possible draw back of this method is the additional memory and inter-processor communication overhead required for implementation. Additionally, small time steps may be required to ensure stability and accurate results, increasing the overall simulation time [23].

A recent study investigating the over-stiffness and over-damping errors highlighted by the aforementioned works has been carried out by Chow et al. [24]. They compared wall impact collisions of ellipsoidal particles, specifically, the dynamics of an analytically defined ellipsoid particle and an MS-DEM ellipse. The authors then proposed two methods to mitigate the effect of over-stiffness and over-damping. One method is an adjustment of force model parameters before running a simulation, similar to the suggestions of Kodam et al. [22]. Therefore, it suffers from the same weaknesses, i.e. accurately carrying out a calibration procedure for irregular particle interactions. The second method Chow et al. [24] proposed is similar to the incremental approach proposed by Höhner et al. [23]. The former approach was moderately successful at mitigating errors, whilst the latter was shown to be highly effective for the contact models and scenarios investigated.

The proposed solutions of three currently identified errors that can occur when using the MS-DEM, are summarised in Table 1.

2. Aims and methods

Despite the amount of previous work aimed at addressing short comings with the MS-DEM, as will be shown in the remainder of this study, there is still scope for improving the proposed methods accounting for the identified over-stiffness and over-damping effects. As such, this work aims to expand on the previous works investigating the validity of contact models for the MS-DEM in several ways. Firstly, All of the previous works focus on particle–wall interactions, whereas in this work, the more general case of inter-particle collisions is considered. Additionally, all of the previous works have focused on convex particles, i.e. only one collision point is present at any given time. In the current study, concave and convex particle interactions are investigated as outlined in Section 4. The analysis conducted is aimed to be the most general evaluation performed on MS-DEM contact models so far, as linear and non-linear models are investigated along with tangential forces and the resulting effects on friction. This includes an in depth analysis of contact surface areas which has not been addressed in the context of the MS-DEM. Moreover, the errors with the MS-DEM uncovered and discussed in this work are investigated rigorously with analytical solutions as well as simulations, with the proposed solutions in this work intended to be as general as possible. Finally, the merits and deficiencies of the previously proposed solutions to the already documented errors for the MS-DEM are discussed with comparison to the newly proposed solutions.

The testing procedures used for the simulations in this work are highly idealised by design, as this allows fair comparison to analytical results. Additionally, these idealised collision scenarios allow for easier identification of errors, as more complex scenarios could potentially contain multiple sources of error. Also, where appropriate, discussion of errors and solutions is given in the context of less idealised collision scenarios. This study is structured in the following manner. To begin, the contact models under consideration will be presented, along with a discussion of the MS-DEM algorithm in Section 3. Then the types of contact which can occur in an MS-DEM collision will be discussed in Section 4. Following this, the simulation procedures to investigate various normal collision scenarios will be introduced in Section 5, with analytical derivations and their respective results given in Appendices A and B. The testing procedures for evaluating the effects of contact area topology are outlined in Section 6, including an investigation of tangential and frictional forces, followed by the results of those tests. A summary of all errors found in the preceding sections is given in Section 7, before solutions to these errors are proposed in Section 8. Using all of the test cases outlined for this work, a comparison of the efficacy of the newly proposed solutions with the previous suggestions given in the literature is provided in Section 9. Numerical considerations for the proposed solutions are discussed in Section 10. Finally, in Section 11, considerations for future areas of investigation and conclusions are given.

3. Contact models and the MS-DEM algorithm

3.1. Linear models

Two linear spring dash-pot models will be investigated in this work and are defined here for spherical interactions. Both use the same spring/conservative forces, with the forms differing with respect to the damping term. The first of the linear spring dash-pot models, Eqs. (1) and (2), uses a velocity dependent damping term whilst *explicitly* using the reduced/effective mass (reduced and effective will be used interchangeably), m_e, of two interacting particles i and j which can be defined with $m_e = m_i m_j/(m_i + m_j)$. The normal and tangential forces obtained from this model are given by

$$\vec{F}_{ij}^{n} = k_n \delta_{ij} \vec{n}_{ij} - \gamma_n m_e \vec{\dot{\delta}}_{ij}^{n}, \tag{1}$$

and

$$\vec{F}_{ij}^{t} = -k_t \vec{S} - \gamma_t m_e \vec{\dot{\delta}}_{ij}^{t}, \tag{2}$$

respectively, where δ_{ij} is the overlap between particles i and j; $\vec{n}_{ij}$ is the unit normal vector in the direction of the line connecting the centres of particle j to i; and k_n and k_t are spring stiffness constants acting in the normal and tangential directions respectively [25]. The normal and tangential damping constants are given by γ_n and γ_t respectively. The respective normal and tangential relative velocities are denoted by $\vec{\dot{\delta}}_{ij}^{n}$ and $\vec{\dot{\delta}}_{ij}^{t}$, with $\vec{S}$ being the elastic shear displacement which is the tangential analogue of δ_{ij}. The second form of linear spring dash-pot model investigated uses a *purely* velocity based damping mechanism [22], given with

$$\vec{F}_{ij}^{n} = k_n \delta_{ij} \vec{n}_{ij} - \gamma_n \vec{\dot{\delta}}_{ij}^{n}, \tag{3}$$

and

$$\vec{F}_{ij}^{t} = -k_t \vec{S} - \gamma_t \vec{\dot{\delta}}_{ij}^{t}, \tag{4}$$

where all symbols share meanings with Eqs. (1) and (2), with the discrepancy that the damping constants of the two models must use different dimensions (i.e. time T, length L and mass M) with $[\gamma_n, \gamma_t] = T^{-1}$ for the m_e based terms, whereas $[\gamma_n, \gamma_t] = T^{-1}M$ when purely velocity based damping is employed. For both forms of model the stiffness constants have identical dimensions of $[k_n, k_t] = T^{-2}M$.

3.2. Non-linear models

Non-linear Hertzian contact models, using an explicit reduced mass damping term for normal and tangential forces, are determined for spherical interactions as

$$\vec{F}_{ij}^{n} = \sqrt{\delta_{ij} R_e}\left(k_n \delta_{ij} \vec{n}_{ij} - \gamma_n m_e \vec{\delta}_{ij}^{n}\right), \tag{5}$$

and

$$\vec{F}_{ij}^{t} = \sqrt{\delta_{ij} R_e}\left(-k_t \vec{S} - \gamma_t m_e \vec{\delta}_{ij}^{t}\right), \tag{6}$$

respectively, where $R_e = r_i r_j/(r_i + r_j)$ is the effective radius, with the radii of contacting particles i and j given as r_i and r_j respectively [26,27]. Meanwhile the purely velocity based damping models are given with

$$\vec{F}_{ij}^{n} = \sqrt{\delta_{ij} R_e}\left(k_n \delta_{ij} \vec{n}_{ij} - \gamma_n \vec{\delta}_{ij}^{n}\right), \tag{7}$$

and

$$\vec{F}_{ij}^{t} = \sqrt{\delta_{ij} R_e}\left(-k_t \vec{S} - \gamma_t \vec{\delta}_{ij}^{t}\right). \tag{8}$$

All other symbols are perfectly analogues to those in the linear models, but the dimensions of the model parameters are modified accordingly. The stiffness constants for both models have dimensions $[k_n, k_t] = L^{-1}T^{-2}M$, for the m_e based model the damping parameters have dimensions $[\gamma_n, \gamma_t] = L^{-1}T^{-1}$ and for the purely velocity based damping model the parameter dimensions are $[\gamma_n, \gamma_t] = L^{-1}T^{-1}M$. Additionally, it is noted that Hertzian models were developed such that parameters can be calculated directly from material properties of the interacting particles, see Brilliantov et al. [26] as an example, rather than calibrated from experiment as is common for the linear models. Moreover, when the viscoelastic damping component is excluded from the non-linear models (analysed in Section 5.5) the classical Hertz–Mindlin normal and tangential force models are recovered [27].

For the remainder of this work, the following nomenclature will be used to distinguish the different forms of model outlined above. For the linear models explicitly using an effective mass -Eqs. (1) and (2)- will be referred to as Model M. Meanwhile the non-linear models explicitly using an effective mass -Eqs. (5) and (6)- will be referred to as Model NLM. Similarly, the linear -Eqs. (3) and (4)- and non-linear models -Eqs. (7) and (8)- using a purely velocity dependant damping mechanism will be referred to as Model V and Model NLV respectively. For all cases, where required, distinction between the normal and tangential forces will be made explicitly.

3.3. Friction

In conjunction with the linear and non-linear models Eqs. (1) to (8), a Coulomb friction coefficient μ_p is often employed to model a stick and slip behaviour which is investigated in this work. This is done by requiring an effective tangential force $F'^{t}_{k,ij} = \min\{\|F^{t}_{k,ij}\|, \mu_p \|F^{n}_{k,ij}\|\} t_k$, where $t_k = F^{t}_{k,ij}/\|F^{t}_{k,ij}\|$ and $k = [1, 2, 3]$ is the given direction in Cartesian coordinates (x, y, z).

3.4. MS-DEM algorithm: Force summation

Interestingly, the majority of specifics regarding a given MS-DEM algorithm are not actually relevant as a source of any of the errors discussed in this work. In particular, the solution of particle kinematics plays no role, i.e. the handling of rotation matrices/quaternions or the specific time integration technique. Interested readers can consult the following sources for information of how the kinematics of such problems can be solved [15,28]. The only part of the MS-DEM algorithm contributing to the source of errors (will be made clearer later), is the force summation procedure between particles, i.e. after all particle contact points have been identified, the following formula is applied

$$\vec{F}_{AB} = \sum_{c=1}^{N_c} \vec{F}_{AB}^{c}, \tag{9}$$

where $\vec{F}_{AB}$ is the total force acting on the MS-DEM particle A from MS-DEM particle B, the superscript c denotes a contact point, specifically a contact between a pair of interacting constituent spheres, with N_c the total number of contact points between A and B. An important point to note here is that this procedure is found not only for the MS-DEM, but many other techniques for simulating non-spherical particles. This includes polyhedra methods [29] and for rigid particles constructed with non-spherical constituents [30]. As such, the sources of error and many of the solutions given here may generally valid for these methods in addition to the MS-DEM.

4. Types of multi-sphere contacts

An important distinction made in this work is the identification of two types of MS-DEM contact. The first of which has been termed here as a computational multi-contact point (see Fig. 1(a)). For this species, multiple constituent spheres are simultaneously involved in a contact, that is intended to represent a single real/natural contact point. The second species of contact has been called the natural multi-contact point (see Fig. 1(b)). In this scenario, real distinct contacts are detected as may occur at local concavities.

The computational multi-contact point was the subject of the previous discussed MS-DEM validity studies (see Section 1), though the natural multi-contact scenario has not been thoroughly investigated. As will be discussed in depth later, the type of contact has a significant impact on the form of error that can be encountered and therefore the respective solution.

5. Collision testing and analytical solutions

5.1. Testing procedures

Three different particle–particle collision tests: A, B and C, have been developed to investigate normal collision scenarios. For Case A, a normal collision of particles that contain N_s non-overlapping constituent spheres, is set-up such that there are $N_c = N_s$ contact points as shown in Fig. 2(a). Case A, is designed to be an idealised representation of a natural multi-contact point problem. For this test case, the ideal/correct results expected are of identical dynamics in comparison to the spherical benchmark set-up in the same configuration (see Fig. 2(c)), in other words, a dynamic response independent of N_s should be obtained. This is because in a normal collision using this test case, the contact properties (area, overlap, relative velocities and model parameters) are identical for each contact point c, which should therefore each yield the same force responses as that of a single sphere, i.e. regardless of the model $\vec{F}_{AB} = N_c \vec{F}_{AB}^{c} = N_c \vec{F}_{sphere}$ where $\vec{F}_{sphere}$ is the force resulting from the spherical benchmark. Moreover, the mass of each MS-DEM particle is proportional to the number of constituent spheres. Therefore, the proportional increase in force and mass should produce the same dynamic response as a spherical benchmark.

For Case B, a normal collision of particles that contain N_s non-overlapping constituent spheres is set-up such that there are $N_c = 1$ contact points as demonstrated in Fig. 2(b). The utility of Case B is to investigate the effect of increasing particle mass, whilst maintaining the same model parameters and collision properties (contact area etc.). Experimental collision tests between spherical particles, show a decrease in coefficient of restitution and increase in energy loss as the masses of the spheres is increased as shown by Goldsmith [31] and Aryaei et al. [32]. A caveat is that the effective radii of the interacting spheres was increased commensurately, with no experiments fixing the contact radii whilst increasing the particle mass readily available. However, significantly increasing the mass of the interacting particles has a comparatively small impact on the change on R_e. For example, by rearranging the calculation of a sphere volume given by $V_{sphere} = 4/3\pi r^3$, it is easily shown that doubling the mass of spheres in a given collision (assuming constant density) only increases the effective radius

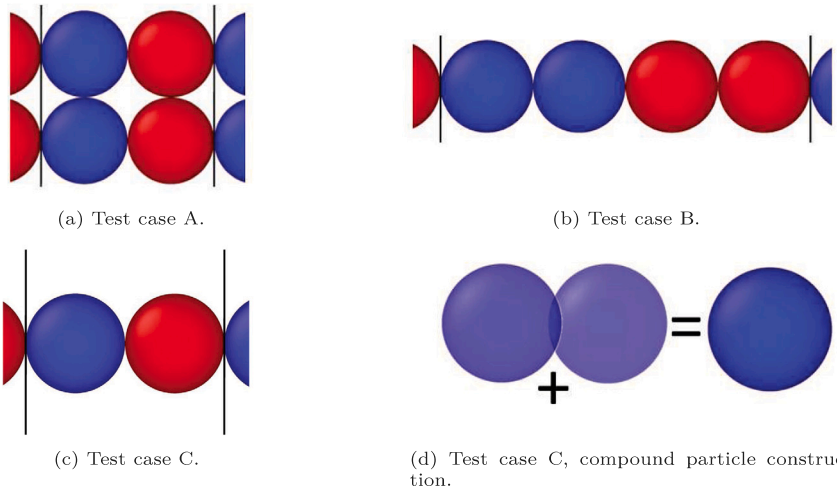

(a) Test case A. (b) Test case B. (c) Test case C. (d) Test case C, compound particle construction.

Fig. 2. Examples of $N_s = 2$ for all test cases, where the red spheres and blue spheres distinguish the MS-DEM particles. (a) $N_c = N_s = 2$. (b) $Nc = 1$ and $N_s = 2$. (c) For Case C, $N_s = 2$ and $N_c = 4$, alternatively when representing the spherical benchmark $N_s = N_c = 1$. Each case is configured such that only 2 MS-DEM particles are in contact at a given time. The black lines indicate the periodic boundaries, with the periodic images visible on either side.

by $\approx$ 26%. Moreover, the theoretical elastic–plastic collision model of Thornton [33], predicts that increasing the effective mass should decrease the coefficient of restitution, even if R_e is held constant. As such, it is assumed here that the qualitative findings of the experimental data would remain unchanged for Case B, hence an increase in damping is assumed to be the accurate behaviour.

Finally, for Case C, a normal collision of 'compound' spheres is performed, with compound spheres defined as having N_s constituent spheres of identical diameter with no spacing between their centres. This test case is shown in Fig. 2(c) and the construction of the compound shape is given in Fig. 2(d). This test case is designed to be an idealised representation of a computational multi-contact problem, specifically contacts between extremely high fidelity surface representations. Importantly, Case C is chosen to remove any discrepancies caused by artificial roughness and results in $N_c = N_s^2$ contact points. In addition to these test cases, a classical spherical DEM benchmark is generated for comparison using a set-up identical to that presented in Fig. 2(c). The correct physical response expected of Case C is the same criteria as Case A, i.e. identical to the spherical benchmark.

All test cases are imparted with the same initial relative velocity, $\dot{\delta}_0$, for which all results (non-dimensional quantities) presented are independent. The simulations are quasi-one dimensional with only one degree of freedom explored, with all particles three dimensional. All the simulations are performed using periodic images (see Fig. 2) with the particles always involved in contact with either a particle in the domain or with a periodic image, which will produce sinusoidal velocity responses for a convenient comparison with analytical results. For all test cases, the velocity responses, coefficient of restitution $e = |\dot{\delta}'/\dot{\delta}|$, with $\dot{\delta}$ and $\dot{\delta}'$ the pre- and post-collision velocities respectively, and the duration of contact, t_c, resulting from each collision are investigated. These tests are carried out for $N_s \in [2...20]$, with N_c varying accordingly for each test case. All the contact models are investigated numerically and compared against the classical spherical DEM results (only normal forces are considered for these tests). Analytical derivations are given in Appendix A for the linear models to compliment the simulation results and determine the sources of error. In addition, a breakdown of each force component (conservative and damping) for these tests is performed to identify errors. All the simulations are performed using LAMMPS (Large-scale Atomic Molecular Massively Parallel Simulator) [34], which has been modified for this work.

Cases A and B as well as the spherical benchmark use identical sphere diameters and densities (for all models). Case C uses the same diameter as the other test cases, however, the density of each constituent sphere is adjusted so that the total mass of the particle is equivalent to the spherical benchmark. All model parameters are selected such that they yield a restitution coefficient $e = 0.9$ for the spherical benchmark using a given model. Keeping the same parameter values for all tests is important to establish the forms of error which can be incurred, as the effect of particle morphology can only be identified if all other control variables remain constant. For Model M and Model V, the γ_n values are found for a given e and k_n using the appropriate solutions provided in Appendix A. For Model NLM and Model NLV, the normal stiffness and damping parameters are found numerically for the spherical benchmark for the given $\dot{\delta}_0$. For the test cases introduced later which consider tangential forces (see Section 6), the tangential parameters for the linear and non-linear models are calculated as $k_t = 1/2k_n$ and $\gamma_t = 2/7\gamma_n$. All the other experiments and analytical work carried out later in the study use identical parameter values to those determined for these tests.

5.2. Analytical comparison

For Cases A–C, linear second-order homogeneous differential equations can be constructed to describe the particle system and are developed for each linear model and test case, see Table A.4. The main purpose of this analytical treatment, in contrast to depending solely on simulations, is to provide a rigorous understanding of the potential errors. Moreover, the analytical results lend confidence to the data generated from the simulations, as all the analytical results are in agreement with the simulation data. For the remainder of this study, all results pertaining to the analytical solutions (Model M and V) are provided in Appendix B.

5.3. Results and discussion

In this section, the change in e, the relative contact duration t_c^* and the normalised velocity response $\dot{\delta}^*$ are presented for Cases A–C with respect to N_s. The relative contact duration is defined as $t_c^* = t_c/t_{c,sphere}$ where t_c is the contact duration for the given test case and $t_{c,sphere}$ is the contact duration of the relevant spherical benchmark. The normalised velocity response for a given test case and N_s is given by $\dot{\delta}^* = \dot{\delta}/\dot{\delta}_o$ where $\dot{\delta}_o$ is the particle velocity at $t = 0$. Moreover, the normalised velocity responses are plotted with respect to a normalised time given by $t^* = t/t_c$ where t is the simulation time and t_c is the contact duration of the given test scenario found in Figs. 3(c) and 3(d). Therefore, $t^* = 5$ is the time at which a fifth collision has been completed using the

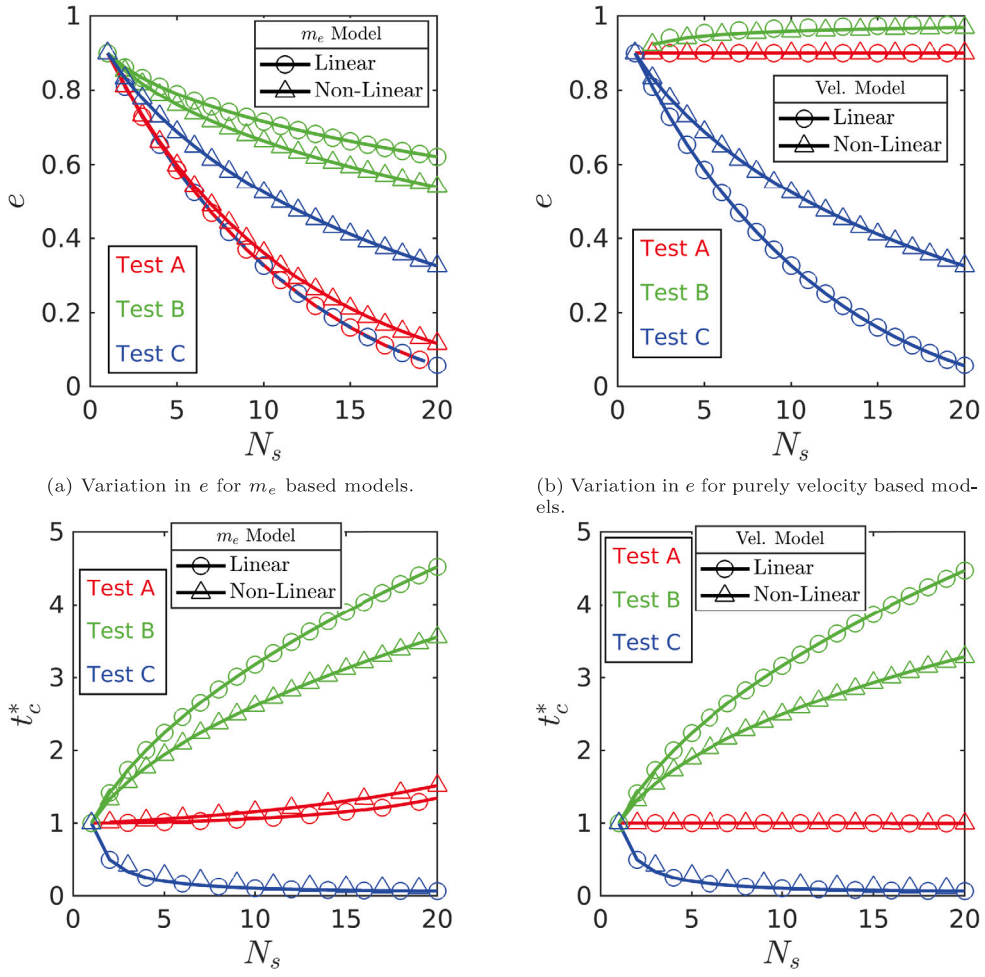

(a) Variation in e for m_e based models.

(b) Variation in e for purely velocity based models.

(c) Variation in t_c^* using m_e based models.

(d) Variation in t_c^* using purely velocity based models

Fig. 3. Changes in e and t_c^* with respect to N_s for each contact model and all test cases. m_e Model corresponds to Model M and NLM data, with Vel. Model corresponding to Model V and NLV.

periodic configurations shown in Fig. 2. As the tests are quasi-one dimensional and use rigid bodies, each constituent sphere in a given particle has the same velocity response. Similarly, each distinct contact point has the same contact duration. All results, in this and in later sections investigating other test configurations (see, Sections 6 and 9) are extracted from the simulation data.

As a reminder, for Case A, a physically accurate model should produce system dynamics independent of N_s. As such, using Model M, the change in e with respect to N_s, ($N_s = N_c$ for test A) depicted in Fig. 3(a) demonstrates that significant over-damping occurs. Even with just 2 contact points, $N_c = 2$, the coefficient of restitution decreases by approximately 10%. This extreme over-damping is accompanied by a slight increase in contact duration as is evidenced in Fig. 3(c). The extremity of this dissipation is also evident in the velocity responses shown in Fig. 4(a). Using Model NLM the results are qualitatively identical to model M, as shown in Figs. 3(a), 3(c) and 4(b). However the over-damping effect is marginally smaller in magnitude than the linear case. Interestingly, Model V or Model NLV results in no deviations with respect to the spherical benchmark for Case A as is shown in Figs. 3(b), 3(d) and 4, i.e. the behaviour is correct. The corroborating analytical results are shown in Figs. B.19 and B.20.

For Case B, an accurate contact model is expected to produce additional damping in comparison to the spherical benchmark. Using Model M with this test case, the change in e with respect to N_s, $N_c = 1$, given in Fig. 3(a), clearly demonstrates additional damping, as e is inversely correlated to N_s. This additional damping is coincident with a significant increase in the contact duration as shown in Fig. 3(c), with the increased damping also evident in the velocity responses as given in Fig. 5(a). As with Case A, Model NLM results in qualitatively very similar behaviour to Model M, with the non-linear results showing a slight increase in damping (see Figs. 3(a) and 5(b)). Therefore, the evident additional damping demonstrates that Model M and Model NLM show accurate physical behaviour. As shown in Fig. 3(b), the inverse of the Model M and NLM behaviour occurs when Model V and NLV are used, i.e. e increases as N_s increases. Meanwhile, Model V and Model NLV both display an increase in contact duration. The effect of the increase in coefficient of restitution on the velocity response of the particles is given in Fig. 5(a). Model NLV shows a qualitatively identical response to Model V, though is slightly less sensitive in terms of the increase in e (see Figs. 3(b), 3(d) and 5(b)). Using the success criteria for the Case B, the behaviour of increasing e demonstrated by Model V and MLV is evidently erroneously/unnaturally under-damping. For Model M and Model V, all the results are corroborated analytically, as shown in Figs. B.19 and B.21.

Finally, for Case C ($N_c = N_s^2$), Model M results in identical over-damping behaviour to Case A, as demonstrated in Figs. 3(a) and 6(a). However, the contact duration significantly decreases as N_s increases, indicating over stiffness (see the following section for more details). Additionally, Model V results in identical behaviour to Model M, as shown in Figs. 3(b), 3(d) and 6(a). The respective non-linear models show identical qualitative behaviour to the linear models. However, Model NLM shows some additional over-damping in comparison to

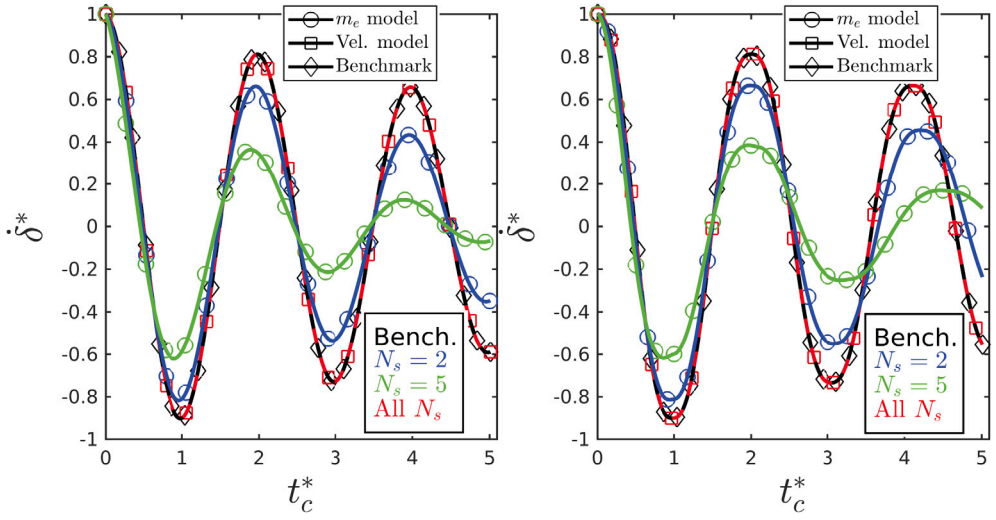

(a) Linear Models (b) Non-Linear Models

Fig. 4. Test A's velocity responses. (a) m_e model corresponds to Model M data, with Vel. model corresponding to Model V. (b) m_e model corresponds to Model NLM data, with Vel. model corresponding to Model NLV. All N_s represents N_s independent results acquired from Models V and NLV. Bench is the spherical benchmark data.

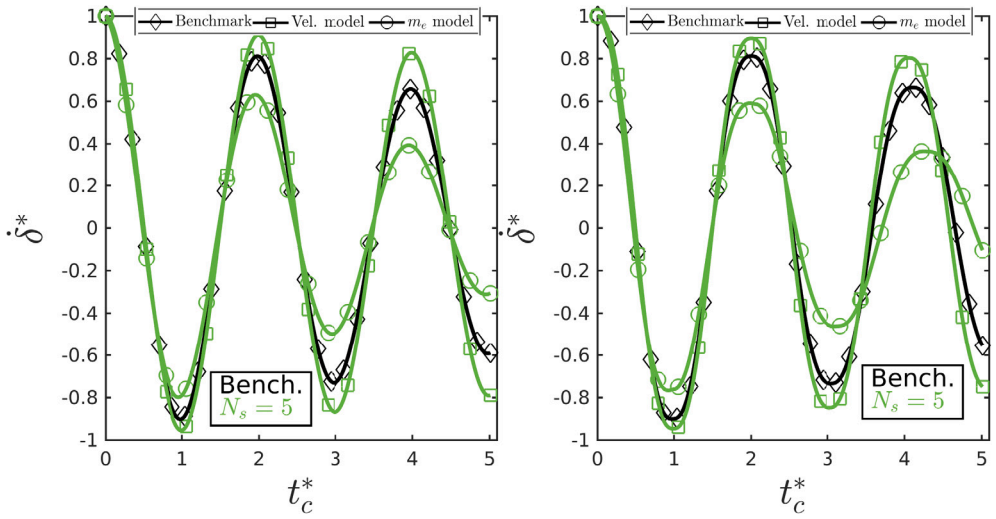

(a) Linear Models. (b) Non-Linear Models.

Fig. 5. Test B's velocity responses, only $N_s = 5$ is shown to improve figure clarity. (a) m_e model corresponds to Model M data, with Vel. model corresponding to Model V. (b) m_e model corresponds to Model NLM data, with Vel. model corresponding to Model NLV. Bench is the spherical benchmark data.

Model NLV as shown in Fig. 6(b). Again the analytical results confirm the findings of the simulation data as shown in Figs. B.19 and B.22.

In the following subsections the causes of the aforementioned deviations from the spherical benchmarks are discussed by breaking down the relevant components of force, i.e. conservative elastic forces and damping forces for a single collision.

5.4. Analysis of force components

In order to deconstruct the force components, a slight modification is made in the boundary conditions from the original set-up used for the test cases A–C. Each test case is set-up with an identical fixed overlap $\delta = \delta_o$ and no initial velocity as shown in Fig. 7. The evolution of each force component can then be easily compared between each test case for the duration of the contact. The focus here is on the linear models Eqs. (1) and (3) for convenience, with the results verified by the analytical results given in Appendix B. The non-linear models show qualitatively identical results to the linear cases which are shown in Appendix B, but are not discussed here for the sake of brevity. Furthermore, all the results are for normal collisions only, with tangential forces explored in the next section. The analytical solutions require slight modification for this test setup due to the change in boundary conditions which are provided in Appendix A.1.

The force components to be examined are the conservative and damping components, i.e. F^C and F^D respectively. The term "conservative" refers to the terms involving k_n and k_t in Eqs. (1) to (8), while the "damping" refers to the terms that involve γ_n and γ_t. All force components are plotted against the dimensionless overlap, presented as a percentage, given by $\delta^* = (\delta/\delta_o) \times 100$ (see Fig. 7). The particles are initially imparted with an overlap of 5% (relative to the sphere radii). The results are, however, independent of this initial value.

5.5. Conservative forces

For all the test cases, Model M and Model V have identical responses with respect to conservative forces. For Case A, the results in Fig. 8 clearly demonstrate that the resulting conserved forces are larger by

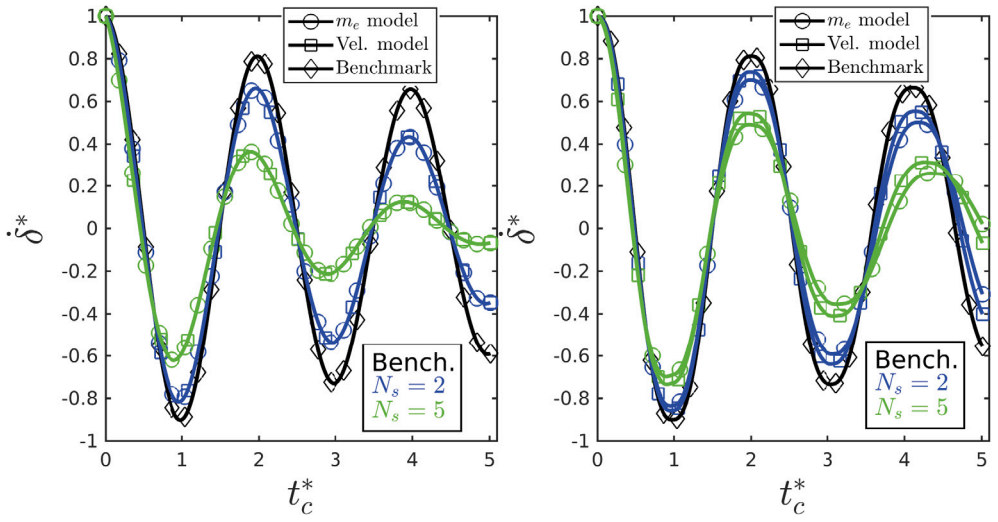

(a) Linear Models. (b) Non-Linear models.

Fig. 6. Test C's velocity responses. (a) m_e model corresponds to Model M data, with Vel. model corresponding to Model V. (b) m_e model corresponds to Model NLM data, with Vel. model corresponding to Model NLV. Bench is the spherical benchmark data.

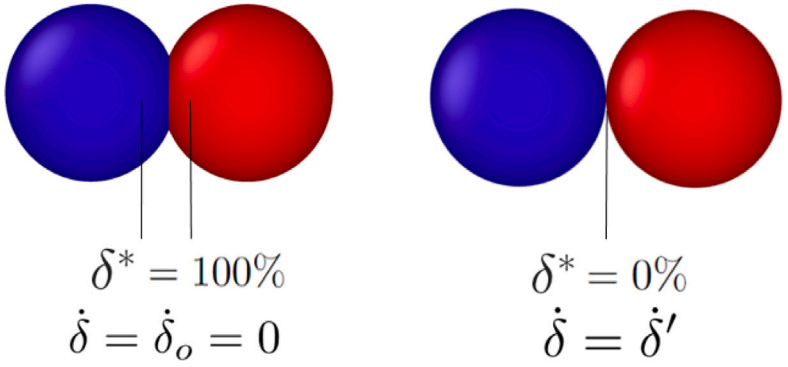

Fig. 7. Force deconstruction test for spherical benchmark (or test C) at both the initial, $\delta^* = 100(\%)$, and final stages, $\delta^* = 0(\%)$, where $\delta^* = (\delta/\delta_o) \times 100$.

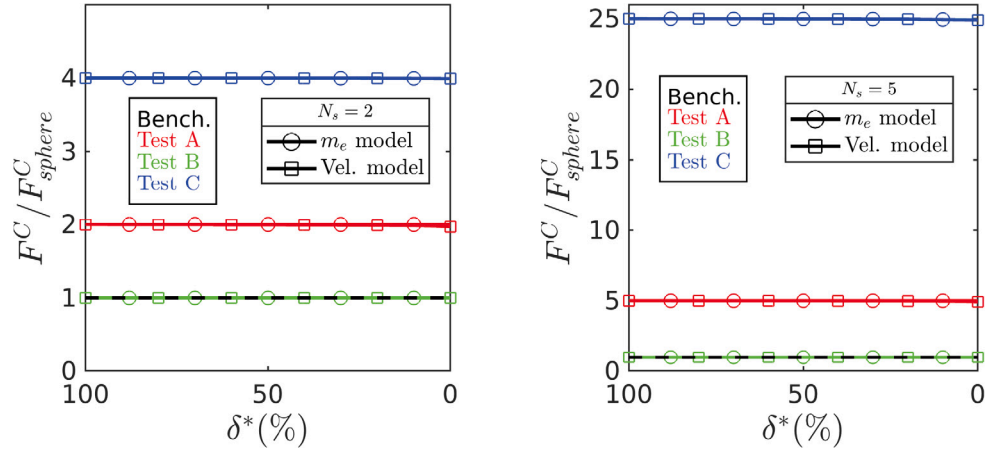

(a) Conservative force responses with $N_s = 2$. (b) Conservative force responses with $N_s = 5$.

Fig. 8. F^C is the conservative force at a given δ^*, with F^C_{sphere} the conservative force of the appropriate spherical benchmark at the same δ^*. In the legends, m_e model corresponds to Model M data, with Vel. model corresponding to Model V. Bench is the spherical benchmark data, for which Model M and Model V produce identical results.

a factor of N_s in comparison to the spherical benchmark with the total conservative force given by $F^C_{AB} = N_s F^C_{sphere} = N_c F^C_{sphere}$, where F^C_{sphere} is the conservative force obtained from the spherical benchmark. However, for this test case, in the context of a natural multi-contact problem, these higher resulting forces should be considered correct. This is because all distinct contact points have identical properties and hence, should produce the same force response as the spherical benchmark. For Case B, the conservative forces are identical to that of the spherical benchmark as would be expected. Meanwhile, Case C demonstrates a conservative force N_s^2 higher than the benchmark

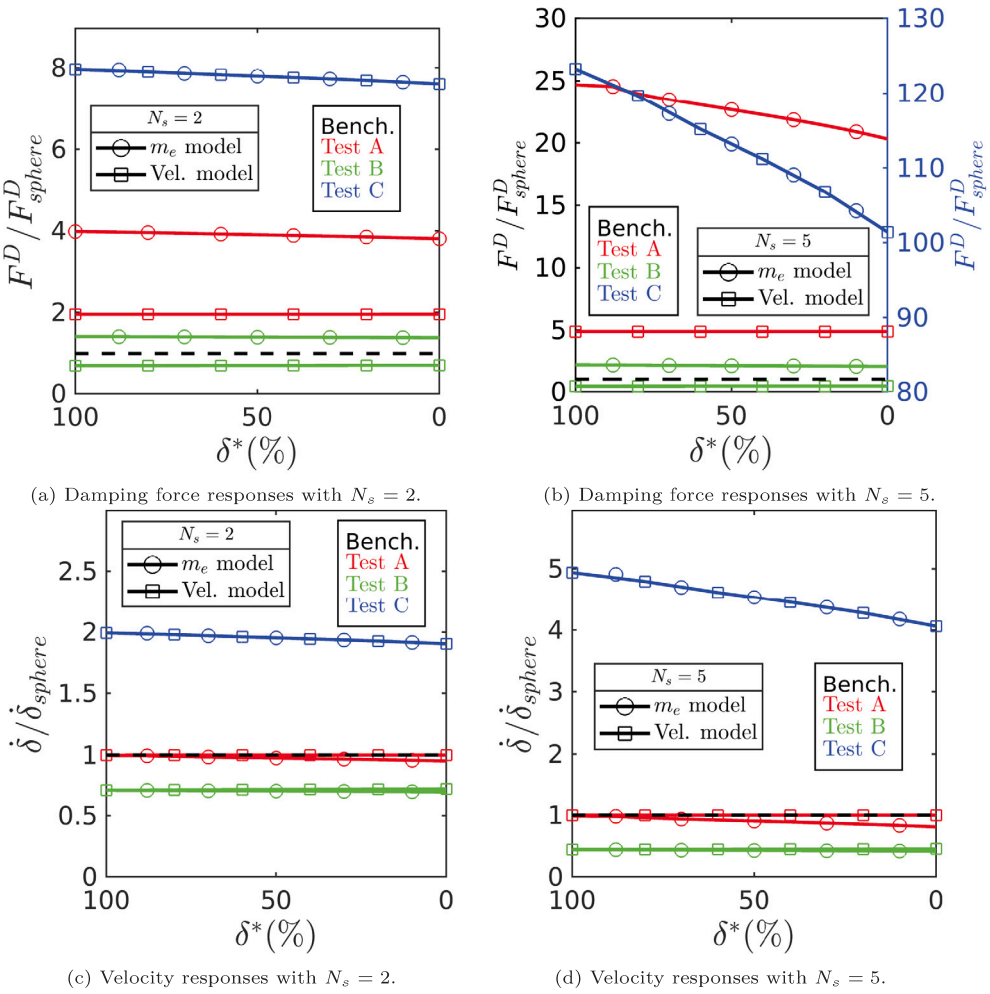

(a) Damping force responses with $N_s = 2$.

(b) Damping force responses with $N_s = 5$.

(c) Velocity responses with $N_s = 2$.

(d) Velocity responses with $N_s = 5$.

Fig. 9. For (a) and (b), F^D is the damping force at a given δ^*, with F^D_{sphere} the damping force of the appropriate spherical benchmark at the same δ^*. For (c) and (d), $\dot{\delta}$ is the relative velocity at a given δ^*, with $\dot{\delta}_{sphere}$ the relative velocity response the appropriate spherical benchmark at the same δ^*. In the legends, m_e model corresponds to Model M data, with Vel. model corresponding to Model V. Bench is the spherical benchmark data, for which Model M and Model V produce identical results.

i.e. $F^C_{AB} = N_s^2 F^C_{sphere} = N_c F^C_{sphere}$. In this instance, a computational multi-contact point is present with the resulting over estimation being unnatural and demonstrating the canonical over-stiffness problem. All of these results are corroborated analytically as shown in Figs. B.23(a) and B.23(b) and the non-linear results are quantitatively identical as shown in Figs. B.25(a) and B.25(b).

5.6. Damping forces

For Case A, as evidenced in Figs. 9(a) and 9(b), Model M shows additional damping by $\mathcal{O}(N_s^2)$. This $\mathcal{O}(N_s^2)$ damping behaviour in comparison to the $\mathcal{O}(N_s)$ conservative behaviour is what results in over-damping as described in Section 5.3. It is not immediately clear why this would be the case from Eq. (1), however focus on the m_e term elucidates the reasoning for this result. Using the MS-DEM summation procedure given by Eq. (9) (for only the damping component) results in $F^D_{AB} = N_c(\gamma_n m'_e \vec{\dot{\delta}}^n_{AB})$, with $m'_e = N_s m_e$ where m_e is the effective mass of the spherical benchmark, reduces the total damped force to $F^D_{AB} = N_s^2(\gamma_n m_e \vec{\dot{\delta}}^n_{AB})$ with $N_s = N_c$ for Case A, which is the source of the $\mathcal{O}(N_s^2)$ disparity in comparison to the spherical benchmark. However, this behaviour is not constant over the duration of contact as is clear in Fig. 9(b), as t_c is increased in comparison to the benchmark. This is demonstrated in Figs. 9(c) and 9(d), where the velocity in comparison to the spherical response decreases slightly towards the end of the contact. For Model V, the damping forces are increased by $\mathcal{O}(N_s)$, which is true also for the conservative forces as described in Section 5.5. As such, with the mass increasing by a factor N_s, there is no change in the overall dynamics of this test case with respect to the spherical benchmark (same values for e, t_c and $\dot{\delta}$) explaining the correct results obtained in Section 5.3. Moreover, in Figs. 9(c) and 9(d) it is evident that the velocity response is identical over the duration of the contact.

For Case B, using Model M, there is an additional damping observed of approximately 30% in comparison to the spherical benchmark as shown in Figs. 9(a) and 9(b). This occurs as the mass (and volume of the particle) has increased in comparison to the benchmark, whilst the conservative force produced must be identical to that of the spherical case as demonstrated in Section 5.5. Therefore, this leads to a relative decrease in $\dot{\delta}$ in comparison to the benchmark as shown in Figs. 9(c) and 9(d). However, this decrease in relative velocity does not decrease the magnitude of damping as may first be expected. The (natural/correct) over-damping in comparison to the benchmark is due to the increase in reduced mass, given by $m'_e = N_s m_e$, which is large enough to account for the additional damping observed in Figs. 9(a) and 9(b) with the total damping force $F^D_{AB} = N_s \gamma_n m_e \dot{\delta} > F^D_{sphere} = \gamma_n m_e \dot{\delta}_{sphere}$. By contrast, Model V shows a decrease in damping force by approximately 30%. This is due to the lower $\dot{\delta}$ obtained relative to the benchmark (Figs. 9(c) and 9(d)) which is simply scaled with the same damping parameter as that of the benchmark, i.e. the total damping force is reduced as demonstrated by $F^D_{AB} = \gamma_n \dot{\delta} < F^D_{sphere} = \gamma_n \dot{\delta}_{sphere}$.

Finally, Case C using Model M and Model V results in substantial over-damping on the $\mathcal{O}(N_s^3)$. For this test case, as shown in Figs. 9(c) and 9(d), $\dot{\delta} \approx N_s \dot{\delta}_{sphere}$ is caused by the $\mathcal{O}(N_s^2)$ over-stiffness behaviour

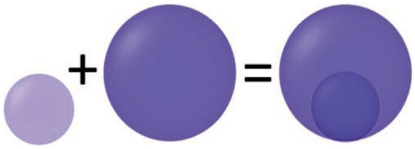

Fig. 10. Test D configuration.

outlined in Section 5.5. Additionally, the total damping force responses as given by Eq. (9), reduces to $F_{AB}^{D} = N_s^2 \gamma_n m_e \dot{\delta} \approx N_s^3 \gamma_n m_e \dot{\delta}_{sphere}$ (with a similar expression for Model V) causing the overall $\mathcal{O}(N_s^3)$ increase in damping. In turn, the damping is approximately $\mathcal{O}(N_s)$ higher than the concurrent conservative forces causing over-damping dynamics in comparison to the benchmarks whilst simultaneously being over-stiff.

Again, for all the results shown here, analytical verification is shown in Figs. B.24(a) to B.24(d), with qualitatively identical results obtained for Model NLM and Model NLV as shown in Figs. B.26(a) to B.26(d). These qualitatively similar responses obtained for the non-linear models with respect to the linear models, cause the qualitative similarity between the linear and non-liner models observed in the e, t_c^* and $\dot{\delta}^*$ results given in Section 5.3. Before moving on to discuss any possible solutions of the errors outlined in this and the preceding section, focus is given to the effect of area topology, tangential forces and frictional dynamics.

6. Area topology, tangential forces and friction testing

6.1. Testing procedures

One potential issue that has not been explored is the effect of area topology on force responses with the MS-DEM, which is relevant for the non-linear models given by Eqs. (5) and (7). Therefore, only non-linear results are presented, with all the data extracted from simulations. To investigate the effect of surface areas, a new test case, D, has been set-up, see Fig. 10. The reason for choosing this test case, is that high constituent sphere overlaps with variable radii could be the best method to approximate a given morphology with high fidelity. Case D is very similar to that of Case C, however, the construction is performed with particles using variable radii as shown in Fig. 10.

Only the case of $N_s = 2$ is investigated, with one outer particle with identical diameter to those used in the previous test cases i.e $r = r_{sphere}$, where r_{sphere} is the radius of the spherical benchmark. The second particle is given a radius of $r = r_{sphere}/2$, and positioned so that the outer edges of both particles are in contact. Case C is then directly compared with Case D using the non-linear models. They are first compared using the same force deconstruction procedure used in the previous section(s). Following this, both tests are used to investigate the effect of friction with simulation set-up shown in Fig. 11. In this set-up, the particles are given a fixed overlap, before being moved relative to each other tangentially at a constant speed. This allows for determination of the effect of the area topology on tangential forces and therefore friction behaviour. All test cases uses a inter particle friction coefficient of $\mu_p = 0.5$. For the results shown, only Model NLM is presented as Model NLV results in qualitatively identical behaviour, with identical sources of error as will be discussed shortly.

6.2. Results

As shown in Fig. 12(a), the conservative force response of Case C is 4 times higher than that of the spherical benchmark, meanwhile Case D has a force of approximately 3.3 times higher than the benchmark case. Therefore, the different total contact areas which are encoded within Eq. (5) by the $\sqrt{\delta_{ij} R_e}$ term, must be having a non-trivial impact on the force responses. As the δ_{ij} are the same for all contacts at $t = 0$, the differences (in general) between the total areas of each test case can be quantified with $\sqrt{R_{e,AB}} = \sum_{c=1}^{N_c} \sqrt{R_{e,c}}$ where $R_{e,AB}$ is the total computed effective radius of the MS-DEM particles as would be found using Eq. (9) and $R_{e,c}$ is the effective radius of a specific contact. For Case C, $\sqrt{R_{e,AB}} = 2\sqrt{2}\sqrt{r_{sphere}}$ whilst Case D results in the lower value $\sqrt{R_{e,AB}} = 2.36\sqrt{r_{sphere}}$, explaining the difference in the force responses (see Appendix A.2 for details). For the damping components, analogous behaviour occurs, with Case C showing over damping by ≈ 7.7 times the spherical benchmark, with Case D showing over damping ≈ 6 times the spherical benchmark. The higher over-damping in comparison to the over-stiffness is due to the different resulting velocities as discussed in the previous section (see the note on the $\mathcal{O}(N_s^3)$ damping behaviour of Case C given in Section 5.6). The consequences of this area topology effect will be discussed in more detail in the following section. It is worth noting that if the same decompositions are tested using the linear models, test cases C and D would result in identical force responses. As the corresponding overlaps δ_{ij} are identical meaning the same conservative forces would be calculated, with the resulting velocities (and therefore damping forces) being identical.

For the frictional tests, given in Fig. 11, the same over-stiffness behaviour observed in the conservative force decomposition is observed for both the normal and tangential components as shown in Figs. 13(a) and 13(b). This demonstrates that the errors identified so far, are also present in the tangential forms of the contact models. For the tangential component, the forces peak at around $S^* = 20\%$ for both test cases, before decreasing proportionately with the normal forces. Interestingly, despite the previously identified errors with the normal and tangential forces, due to the definition of the friction forces given in Section 3.3, the overall frictional behaviour shown in Fig. 13(c) is entirely correct and is so for all other models and test cases investigated in this work.

Table 2
Newly identified errors and their causes.

Error	Identified cause
Over-damping in natural multi-contact problem.	Use of a traditional effective mass.
Under-damping.	Increasing particle mass, with purely velocity based damping parameters remaining constant.
Contact area topology: Stiffness and damping inconsistencies.	Variable radii present in a computational multi-contact point using non-linear models.

7. Summary of MS-DEM errors

In the previous sections, the test cases have identified a total of 5 types of errors which can occur when using the MS-DEM. Both the previously identified errors of over-stiffness and over-damping are present in computational multi-contact points. In addition to these two types of error, three new types have been identified. The first is over-damping occurring in the case of a natural multi-contact problem using Model M or NLM, caused by additional over-damping at each contact point due to the m_e term. Another newly identified error is the case of *under-damping* which was shown to occur for Case B, when Model V or Model NLV is used. An important observation is that the additional damping occurring for Model M and Model NLM for this test case is identified as being accurate physical behaviour. The final error uncovered in this work is force response sensitivity to contact area topology when using the Hertzian models. These newly identified errors and their respective causes are summarised in Table 2.

8. General solutions for implementing contact models for the MS-DEM

Solutions are proposed for the newly identified errors outlined in the previous section, beginning with the case of over-damping for the natural multi-contact point problem, followed by the area topology errors and the canonical over-stiffness and damping problems.

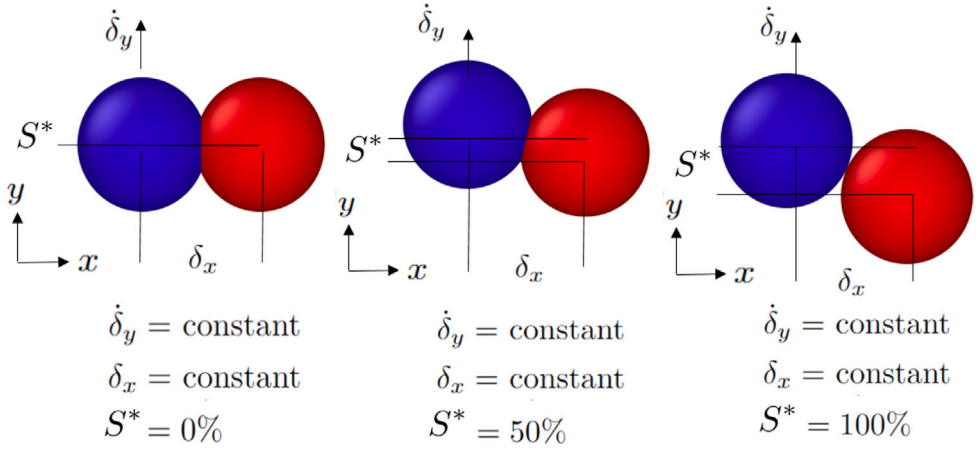

(a) Initial stage of simulation. (b) Mid point of simulation. (c) End of simulation procedure.

Fig. 11. Simulation procedure for evaluating normal and tangential force components. $\vec{S}^* = |\vec{S}|/|\vec{S}_f| \times 100$, where $\vec{S}_f$ is the shear displacement at which the particles lose contact and is the tangential analogue to δ used in the previous force decompositions.

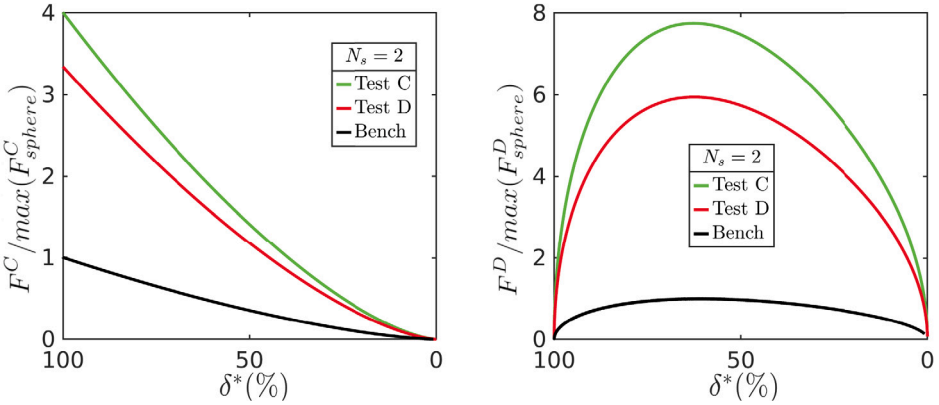

(a) Conservative force component. (b) Damping force component.

Fig. 12. Conservative and damping force decomposition of Case C and Case D with $N_s = 2$, using the set-up given in Fig. 7. Unlike the earlier results shown using this set-up, the forces are normalised against the *maximum* of each force component generated by the appropriate spherical benchmark. This allows for clearer observation of the non-linear responses. δ^* is defined identically to the previous force decompositions. (b) The damping forces are taken as the absolute value i.e. $|F^D|$ before the ratio is taken. Bench is data taken from the spherical benchmark.

8.1. Over-damping effects: the concept of a locally reduced mass

An alternative (though equivalent) definition of reduced/effective mass is $m_e = |\vec{F}_{ij}|/|\ddot{\vec{\delta}}_{ij}|$ where $\ddot{\vec{\delta}}_{ij}$ is the relative acceleration of interacting particles i and j. An important point to note here is that the aforementioned definitions of m_e are for quasi-one dimensional problems with a normal collision only. Focusing on this normal collision scenario in the context of the MS-DEM force summation procedure, substituting the alternate definition results in the following

$$F_{AB} = \sum_{c=1}^{N_c} F^c, \tag{10}$$

assuming m_e is used on a per contact basis,

$$\ddot{\delta}_{AB} m_e = \sum_{c=1}^{N_c} \ddot{\delta}_c m_e, \tag{11}$$

where $\ddot{\delta}_{AB}$ and $\ddot{\delta}_c$ are the relative accelerations between the COM of the MS-DEM particles and the relative accelerations of each contact point respectively, with m_e being the effective mass of the MS-DEM particles. Assuming a normal collision of perfectly rigid bodies, the above equation reduces to

$$\ddot{\delta}_{AB} = \sum_{c=1}^{N_c} \ddot{\delta}_c = N_c \ddot{\delta}_c, \tag{12}$$

for perfectly rigid interacting bodies acting with only translational degrees of freedom $\ddot{\delta}_c = \ddot{\delta}_{AB}$, which results in

$$N_c = 1. \tag{13}$$

This contradiction (N_c can be greater than 1) demonstrates that the use of m_e on a per contact basis in a natural multi-contact scenario is by definition incorrect. To overcome this, the definition of a local effective mass is suggested here. Rather than be limited to the case of a normal collision, the definition of the local effective mass is designed such that normal and tangential force components are handled accurately. An important property of the reduced mass as previously defined is that it is by definition independent of the contact model. Therefore, without loss of generality, only the conservative components of force are required to develop a model for a locally reduced mass. As a starting point the relative acceleration of the surfaces in contact is required, which can be found with

$$\ddot{\vec{\delta}}_c = \ddot{\vec{\delta}}_{AB} + \vec{\omega}_{AB} \times \vec{r}^c + \vec{\omega}_{AB} \times (\vec{\omega}_{AB} \times \vec{r}^c), \tag{14}$$

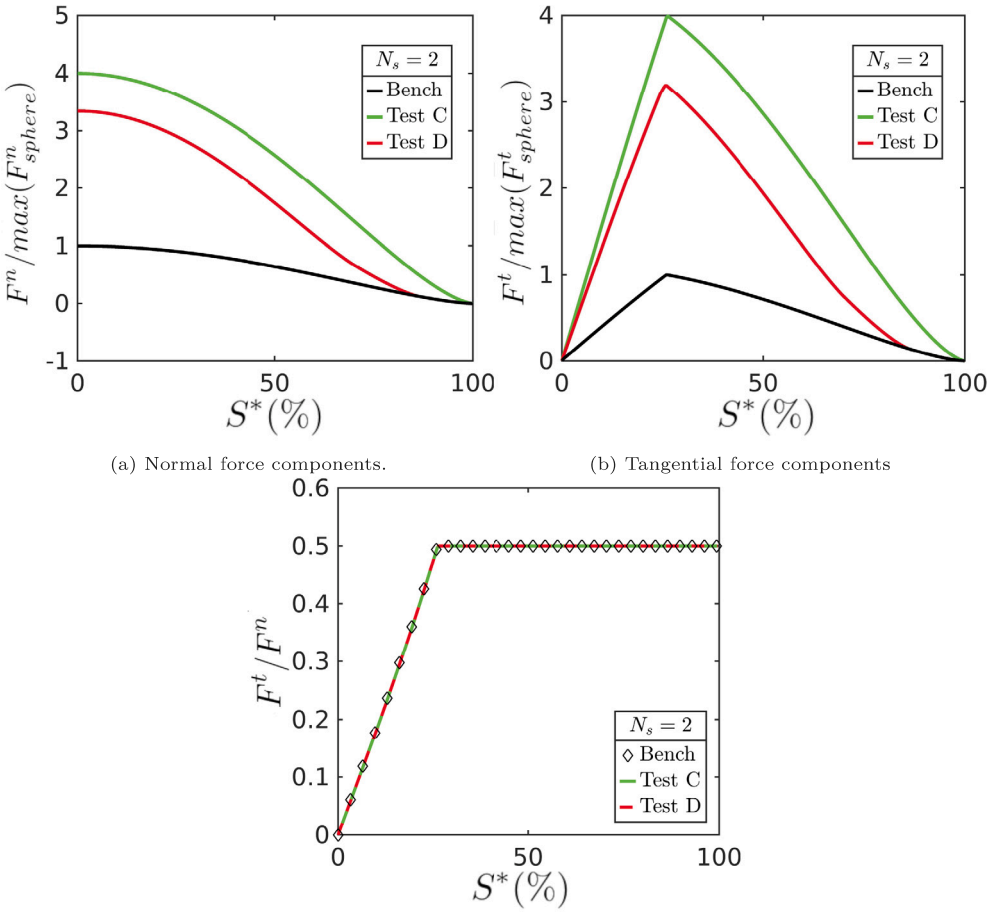

(a) Normal force components.

(b) Tangential force components

(c) Ratio of tangential and normal components, i.e. friction coefficient $\mu_p = 0.5$

Fig. 13. Normal and tangential force decomposition of test Case C and test case D with $N_s = 2$. The forces are normalised against the *maximum* of each force component generated by the appropriate spherical benchmark. This allows for clearer observation of the non-linear responses. The x-axis is defined as $S^* = |\vec{S}|/|\vec{S}_f| \times 100$ (see Fig. 11). Bench is data taken from the spherical benchmark.

where $\vec{r}^c = (\vec{r}^c_B - \vec{r}^c_A)/2$ with $\vec{r}^c_A$ and $\vec{r}^c_B$ being the vectors connecting the COM of the MS-DEM particles A and B to the given contact point c respectively [35]. The relative angular velocity of the MS-DEM particles is given by $\vec{\omega}_{AB}$, with the relative angular acceleration denoted as $\dot{\vec{\omega}}_{AB}$. Using conservative forces only, with the force at each contact is demarcated as $\vec{F}^c_{cons}$, both $\ddot{\vec{\delta}}_{AB}$ and $\dot{\vec{\omega}}_{AB}$ can be determined:

$$\ddot{\vec{\delta}}_{AB} = \frac{1}{m_e}\sum_{c=1}^{N_c} \vec{F}^c_{cons}, \tag{15}$$

$$\dot{\vec{\omega}}_{AB} = \boldsymbol{I}_A^{-1}\left[\sum_{c=1}^{N_c}\left(\vec{F}^c_{cons}\times\vec{r}^c_A\right) - \vec{\omega}_A\times\boldsymbol{I}_A\vec{\omega}_A\right] - \boldsymbol{I}_B^{-1}\left[\sum_{c=1}^{N_c}\left(\vec{F}^c_{cons}\times\vec{r}^c_B\right) - \vec{\omega}_B\times\boldsymbol{I}_B\vec{\omega}_B\right], \tag{16}$$

where $\boldsymbol{I}_A$ and $\boldsymbol{I}_A$ are the inertia tensors of MS-DEM particles A and B respectively. Thus with the above forms, all information required to obtain the relative acceleration at contact, when only considering conservative forces, is readily available within a simulation. Before finally defining the locally reduced mass terms, Eq. (14) needs to be recast into normal and tangential components with respect to a given contact area. Since, Eq. (14) is invariant of the chosen reference frame, it can easily be manipulated to acquire the required components with the normal component given by

$$\ddot{\vec{\delta}}^n_c = \vec{n}^T_c\,\ddot{\vec{\delta}}_c\,\vec{n}_c, \tag{17}$$

where $\vec{n}_c$ is the normal unit vector acting between the constituent spheres centres forming a given contact "c", a superscript "^{T}" denotes a transpose operation. The relative tangential acceleration can then be found with

$$\ddot{\vec{\delta}}^t_c = \ddot{\vec{\delta}}_c - \ddot{\vec{\delta}}^n_c. \tag{18}$$

Finally, the locally reduced mass for normal and tangential force components is defined here as:

$$m^n_c = \frac{|\vec{F}^{c,n}_{cons}|}{|\ddot{\vec{\delta}}^n_c|}, \tag{19}$$

$$m^t_c = \frac{|\vec{F}^{c,t}_{cons}|}{|\ddot{\vec{\delta}}^t_c|}, \tag{20}$$

where $\vec{F}^{c,n}_{cons}$ and $\vec{F}^{c,t}_{cons}$ are the normal and tangential components of the conservative forces acting at contact c.

It is then proposed that for an MS-DEM problem that could contain multiple natural contact points, that the linear and Hertzian models be modified as

$$\vec{F}^n_{ij} = \sqrt{\delta_{ij}R_e}\left(k_n\delta_{ij}\vec{n}_{ij} - \gamma_n m^n_c\dot{\vec{\delta}}^n_{ij}\right), \tag{21}$$

$$\vec{F}^t_{ij} = -k_t\vec{S} - \gamma_t m^t_c\dot{\vec{\delta}}^t_{ij}, \tag{22}$$

and

$$\vec{F}^n_{ij} = \sqrt{\delta_{ij}R_e}\left(k_n\delta_{ij}\vec{n}_{ij} - \gamma_n m^n_c\dot{\vec{\delta}}^n_{ij}\right), \tag{23}$$

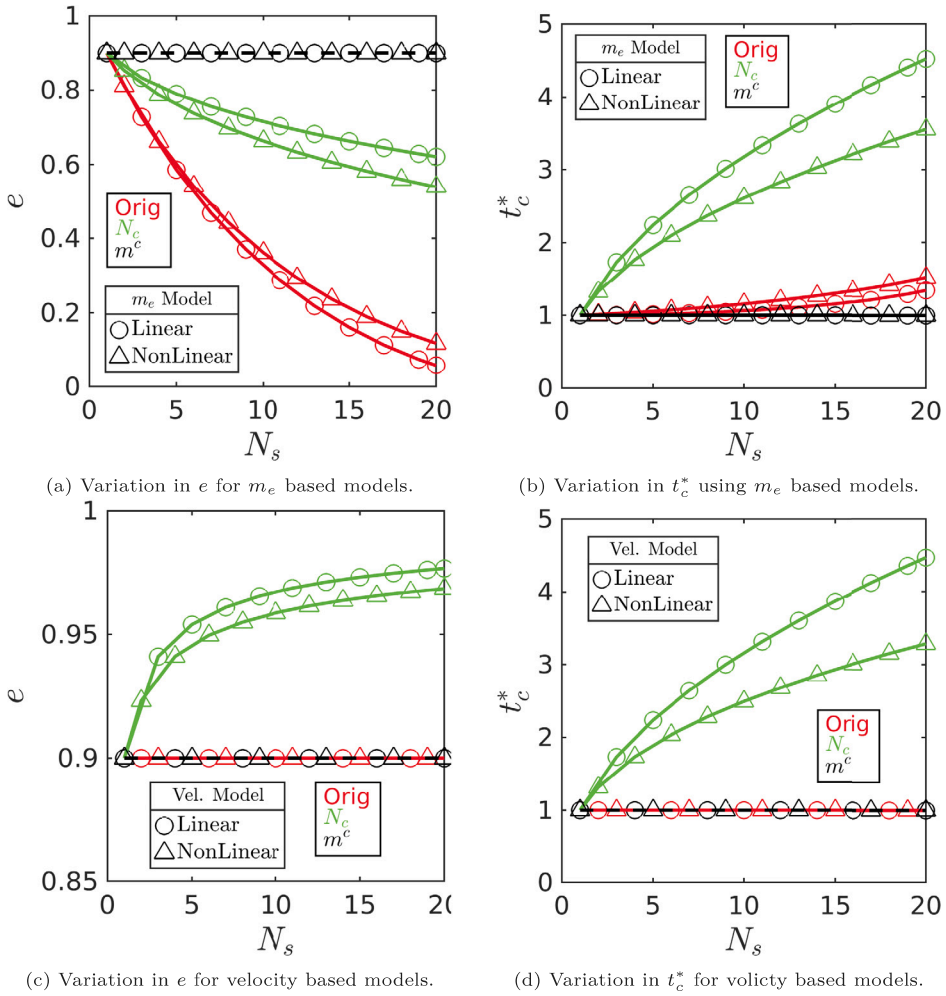

(a) Variation in e for m_e based models.

(b) Variation in t_c^* using m_e based models.

(c) Variation in e for velocity based models.

(d) Variation in t_c^* for volicty based models.

Fig. 14. Comparison of proposed solutions using Case A. All symbols and parameters have the same meaning as described for Fig. 3. Orig, is an unmodified MS-DEM result, with N_c representing the N_c procedure and m^c representing the use of a locally reduced mass. In the legends, m_e Model corresponds to Model M and NLM data, including the locally reduced mass, with Vel. Model corresponding to Model V and NLV.

$$\vec{F}_{ij}^t = \sqrt{\delta_{ij} R_e}\left(-k_t \vec{S} - \gamma_t m_c^t \vec{\delta}_{ij}^t\right). \tag{24}$$

An important note about the above formulations is that they assume binary particle collisions. For dense packings with multiple interacting MS-DEM particles, Eqs. (15) and (16) need to be modified appropriately:

$$\vec{\ddot{\delta}}_{AB} = \vec{\ddot{\delta}}_A - \vec{\ddot{\delta}}_B, \tag{25}$$

with

$$\vec{\ddot{\delta}}_A = \frac{1}{m}\sum_{c=1}^{N_T} F_{cons}^c, \tag{26}$$

where m is the mass of particle A, N_T are contacts between all particles interacting with A. The acceleration of particle B, $\vec{\ddot{\delta}}_B$, is found in an identical manner. The relative angular acceleration given by Eq. (16), only requires the modification of the torque summation, to represent all torques applied at a given time to particle A and B i.e. the total torque on A is given by $\sum_{c=1}^{N_T}\left(\vec{F}_{cons}^c \times \vec{r}_A^c\right)$.

8.2. Under-damping effects

The case of under-damping, is caused by Model V or Model NLV for which the parameter values are determined for particles with a smaller mass. Solving this problem is actually a fairly non-trivial matter. As noted earlier, it is often desirable to maintain the same parameter values in a given study with disparate particle morphologies in order to isolate the effect of the particle shape on system dynamics. Interestingly for this specific issue, the erroneous effects are N_c dependent. As noted earlier, for the Case A, Model V or Model NLV results in the correct physical behaviour. As such, changing parameters based off of the mass a priori would solve the issue for Case B, meanwhile Case A would become erroneous. In order to accurately solve this issue, the damping parameter would need to be altered dynamically over the course of a simulation to ensure that consistent behaviour is observed. Such a procedure is difficult to conceive practically and would simultaneously fail in the goal of maintaining the same parameters. Therefore, similar to [22], it is recommended here to avoid the use of *purely* velocity based damping with the MS-DEM. However, velocity based damping using the local effective mass terms defined in the preceding section is recommended.

8.3. Over-stiffness, over-damping and area topology errors

Using the non-linear models, it is shown that variable radii in a situation where a computational multi-contact problem is present has the potential to significantly change the force response of a given interaction. Both over-damping and over-stiffness would be present, moreover, the exact force response of different MS-DEM structures representing identical surfaces would be different, i.e. the smaller force responses observed for the Case D in comparison to the Case C. This

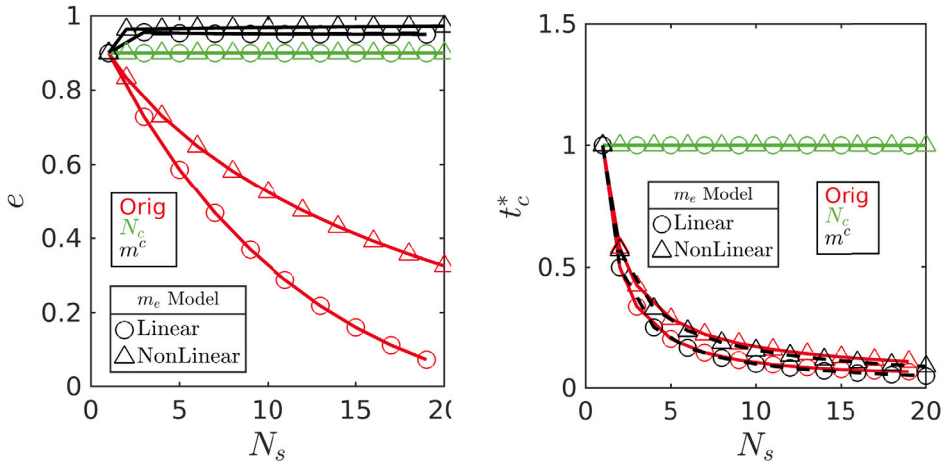

(a) Variation in e using m_e based model.

(b) Variation in t_c^* using m_e based model.

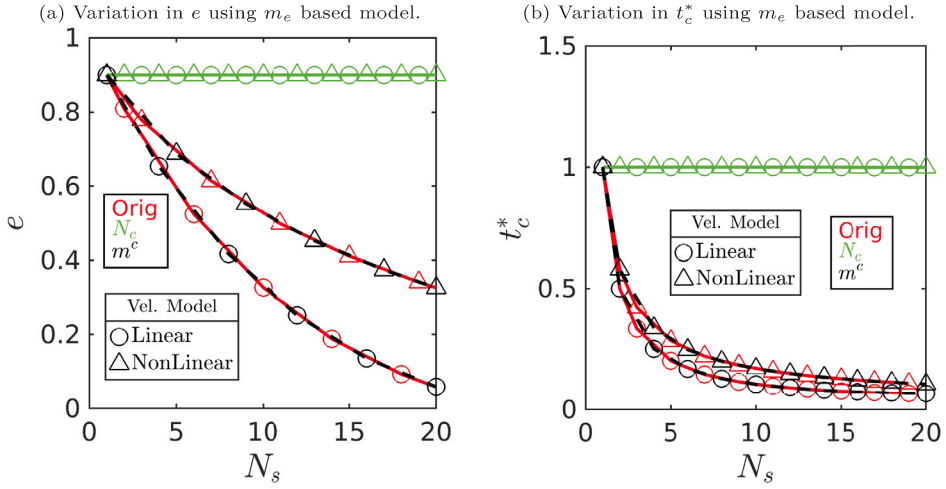

(c) Variation in e using purely velocity based model.

(d) Variation in t_c^* using purely based model.

Fig. 15. Comparison of proposed solutions using Case C. All symbols and parameters have the same meaning as described for Fig. 3. Symbols represent simulation data, for the linear models the solid lines are the analytical predictions, for the non-linear models the lines are included to improve clarity. Orig, represents the unmodified MS-DEM results, with N_c representing the N_c procedure and m^c representing the use of a locally reduced mass. In the legends, m_e Model corresponds to Model M and NLM data, including the locally reduced mass, with Vel. Model corresponding to Model V and NLV.

is likely going to be an issue when high-fidelity particle shapes are defined. In order to address this potential issue, it is proposed that the maximum force generated by the constituent interactions in a computational multi-contact point, is used to represent the force generated from that contact point, written as

$$\vec{F}_{AB} = max(\vec{F}^c_{AB}). \tag{27}$$

Interestingly, a by product of this procedure is that it also acts as a new method for handling the canonical over-stiffness and over damping problems occurring in general computational multi-contact problems as will be shown shortly. For the remainder of this work, Eq. (27) will be referred to as the maximum force procedure or the $max(F^c)$ procedure.

8.4. Previous proposals

Of the previously proposed solutions, the calibration methods will not be investigated here due to their limited practicality as mentioned earlier. Focus will be given to what is called here the N_c procedure, namely the division of contact force or parameter values by the number of contact points N_c. This is the suggestion, originally by Höhner et al. [23], with a nearly identical procedure put forward by Chow et al. [24]. In this work, the N_c based adjustments of Höhner et al. [23],Chow et al. [24] are collected as a single form given as

$$\vec{F}_{AB} = \frac{1}{N_c}\sum_{c=1}^{N_c}\vec{F}^c_{AB}. \tag{28}$$

However, the nature of the test cases explored mean the results from this general procedure would be identical to the specific implementations proposed by both Höhner et al. [23] and Chow et al. [24].

9. Comparison of solutions

9.1. Comparing tests A and C

In order to compare the solutions outlined above, some of test cases developed earlier have been re-investigated using the proposed solutions. The test case A is first investigated with respect to changes in e and t_c as shown in Fig. 14. This represents the ideal natural multi-contact problem for which the locally reduced mass is expected to be a solution.

It is clear that using a local effective mass term as defined in Section 8.1 for Case A, produces consistent results with e and t_c remaining independent of N_s. Using a local effective mass, by definition, has no influence on the Model V or NLV results as shown in Figs. 14(c) and 14(d) which remain correct for this particular test. However, it is worth

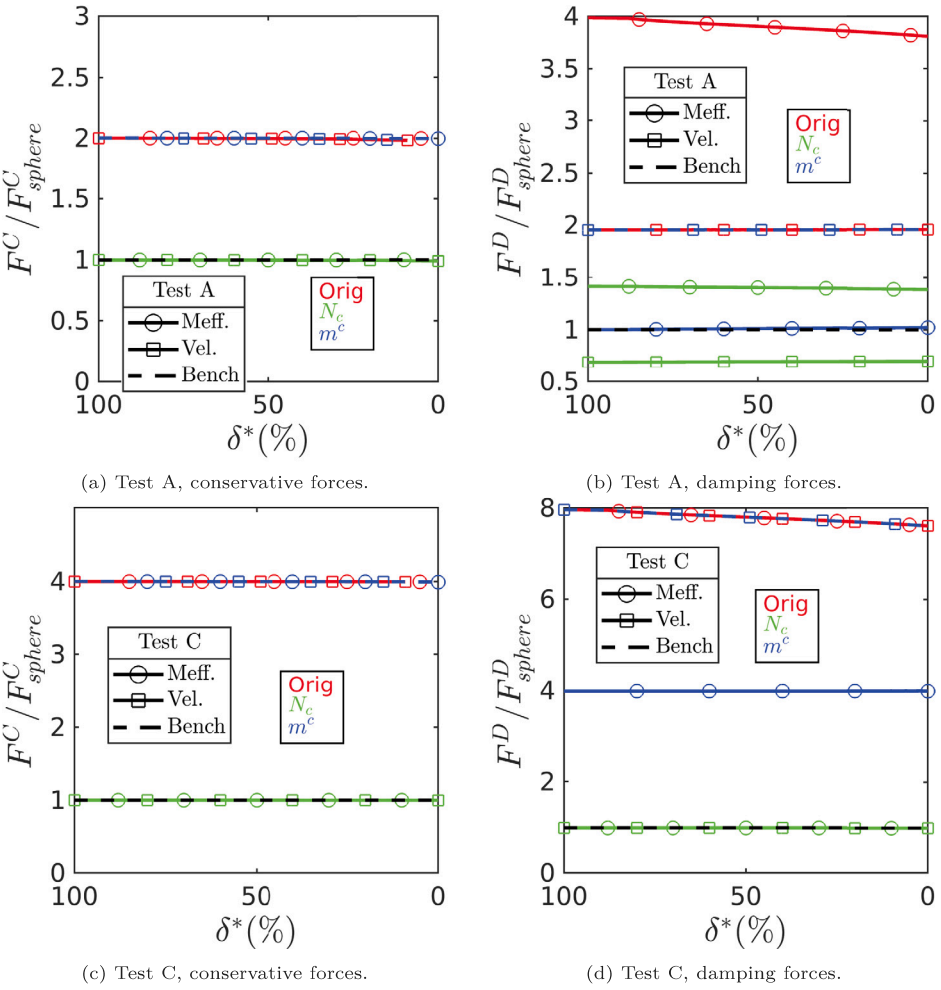

Fig. 16. Conservative and damping force decomposition using the proposed MS-DEM solutions. All symbols and parameters are defined identically to those given in Section 5.4. All results are for $N_s = 2$. Orig, represents the unmodified MS-DEM results, with N_c representing the N_c procedure and m^c representing the use of a locally reduced mass, with Bench being the spherical benchmark results. In the legends, Meff. corresponds to Model M data, including the locally reduced mass, with Vel. corresponding to Model V.

pointing out that the locally reduced mass model, by its definition, would produce accurate results for the Case B behaviour, whilst Model V or NLV would remain erroneous. Looking at the deconstructed force components for the locally reduced mass model as given in Figs. 16(a) and 16(b) (Model NLM and NLV force breakdowns produce identical results as given in Fig. B.27), shows that conservative and damping forces remain proportional to the number of natural contact points, rendering the correct behaviour.

For Case A, the N_c procedure results in erroneous behaviour. Model M and NLM cause excess damping (decrease in e) as shown in Fig. 14(a) and increase in t_c as N_s increases as shown in Fig. 14(b). As demonstrated in Figs. 14(c) and 14(d), using Model V or Model NLV, the N_c procedure causes an increase in e and t_c as N_s increases. These behaviours are explained by the force deconstructions given in Figs. 16(a) and 16(b) (Model NLM and NLV force breakdowns show identical results as given in Fig. B.27). For all contact models, the conservative forces are identical to the benchmark. However, Model M and Model NLM show over-damping in comparison to the benchmark, meanwhile, Model V and Model NLV are under-damped. The explanation for this disparity in damping behaviour is identical to that given for Case B in Section 5.6.

Focusing now on the e and t_c behaviour resulting from changes with N_s Case C, reveals the utility of a N_c procedure. For all models, the N_c procedure produces accurate results, see Fig. 15, with e and t_c independent of N_s. The reasoning for this is evident from the force deconstructions given in Figs. 16(c) and 16(d) (Model NLM and NLV force breakdowns show identical results as given in Fig. B.27), where both the conservative and damping components are identical to that of a single sphere. The locally reduced model, as shown in Figs. 15(a) and 15(b) causes an increase in e with t_c decreasing as N_s increases (Models V and NLV are not effected). The reasoning for this behaviour elucidated from Figs. 16(c) and 16(d) is that the damping is reduced significantly by the use of the locally reduced mass, however, the conservative forces are not treated by the this procedure causing the under-damping.

To summarise briefly, the locally reduced mass model successfully remedies the errors incurred for the case of a natural multi-contact problem but cannot be used to solve a computational multi-contact problem. Conversely a N_c procedure yields excellent results for a computational multi-contact problem with uniform radii, but fails to accurately handle natural multi-contact problems.

9.2. Comparing tests C and D: area topology effects

In this section, the contact area topology testing procedures as described in Section 6 are repeated using the newly proposed solutions. This includes the conservative and damping force deconstruction as well as the normal and tangential deconstruction setups outlined in Section 6. In the previous section, the locally reduced mass was shown to be the solution for natural multi-contact problems. However, by design it is not equipped to solve computational multi-contact problems, and is

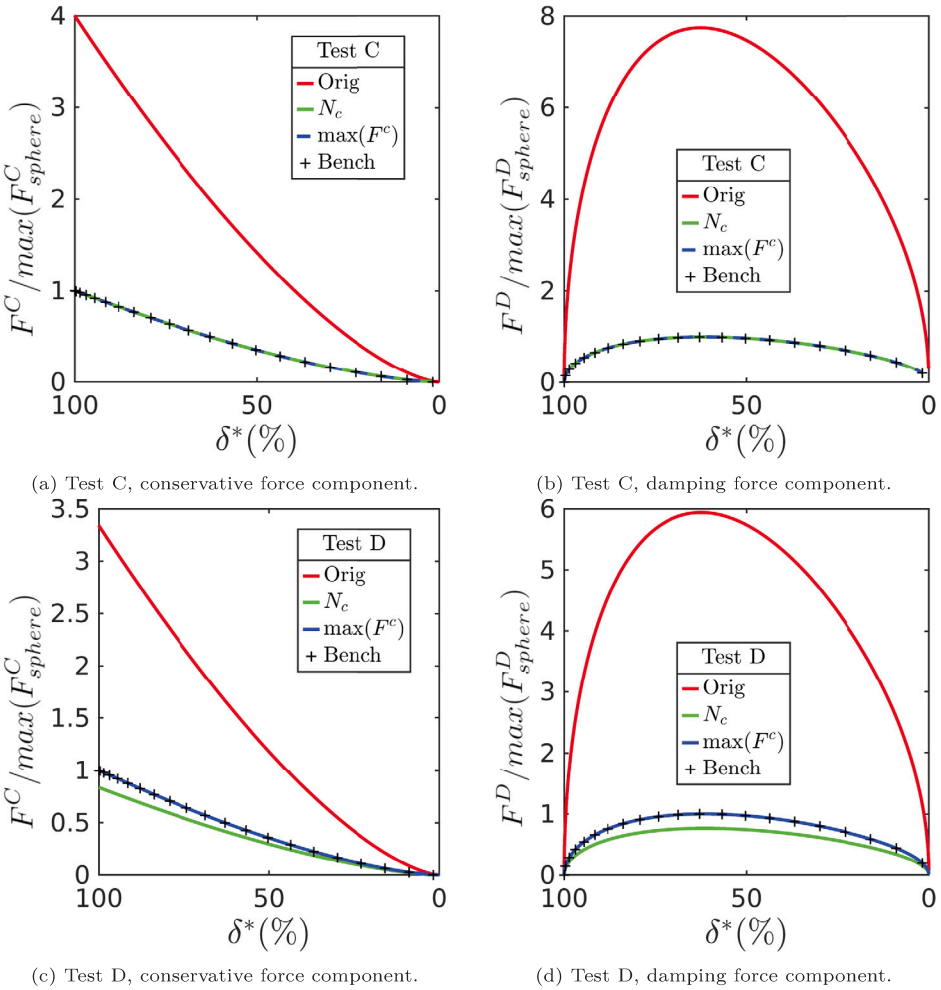

(a) Test C, conservative force component.

(b) Test C, damping force component.

(c) Test D, conservative force component.

(d) Test D, damping force component.

Fig. 17. Conservative and damping force decomposition of Case C and Case D with $N_s = 2$ using the proposed solutions. The forces are normalised against the *maximum* of each force component generated by the appropriate spherical benchmark. δ^* is defined identically to the previous force decompositions. For (b) and (d) the damping forces are taken as the absolute value i.e. $|F^D|$ before the ratio is taken. Orig, represents the unmodified MS-DEM results, with N_c representing the N_c procedure and $max(F^c)$ representing the $max(F^c)$ procedure, with Bench being the spherical benchmark results.

therefore excluded here for comparison. Instead, the $max(F^c)$ procedure is used to compare fairly against the N_c procedure results.

Focusing on the N_c procedure, when a non-linear multi-contact problem in the form of Case C is present, the procedure can accurately predict the conservative and damping force components as shown in Figs. 17(a) and 17(b). This is verified with the normal and tangential force breakdowns for Case C given in Figs. 18(a) and 18(b). However, for Case D, the N_c procedure cannot accurately predict the force responses, as evidenced in Figs. 17(c) and 17(d) in terms of conservative and damping forces and in Figs. 18(c) and 18(d) with respect to normal and tangential forces. In all instances, the N_c division causes an underestimation of the force values. This is caused for Case D, as the total contact area does not have a one-to-one correspondence to N_c unlike Case C, for which the area grows proportionally with N_c accounting for the correct results with the N_c procedure for that particular test case.

In contrast, the $max(F^c)$ procedure, as shown in Figs. 17 and 18, produces results commensurate with the benchmark for all the test cases and force components. To clarify, the $max(F^c)$ procedure solves both area topology inconsistencies as well as general computational multi-contact problems. The reason the $max(F^c)$ procedure works well for Case C is that, by definition, for this case it returns the expected force of a single contact (i.e. the benchmark force response), which was the motivation of the N_c procedure. For Case D, it also has the effect of returning the same benchmark forces, as the larger sphere contact area and resulting force is used which is identical to the benchmark configuration.

10. Numerical considerations

10.1. Implementation

The above proposals are currently implemented for binary particle interactions. Naturally, additional considerations must be made when implementing for large scale systems. Full implementations for both the local effective mass and the $max(F^c)$ procedure will require additional memory and communication overhead in comparison to a standard MS-DEM algorithm. Additionally, to ensure accuracy it is recommended that the above procedures be performed at each time step.

The concept of the local effective mass can be implemented using the following high level scheme, which acts within a standard MS-DEM algorithm as described in [28]:

1. Run standard contact procedure and calculate all conservative forces acting on the particles.
2. Sum all conservative forces and torques acting on the MS-DEM particles and communicate the required information between processors to acquire the total conservative forces.
3. Calculate the translational and rotational accelerations of each MS-DEM particle and store these values.

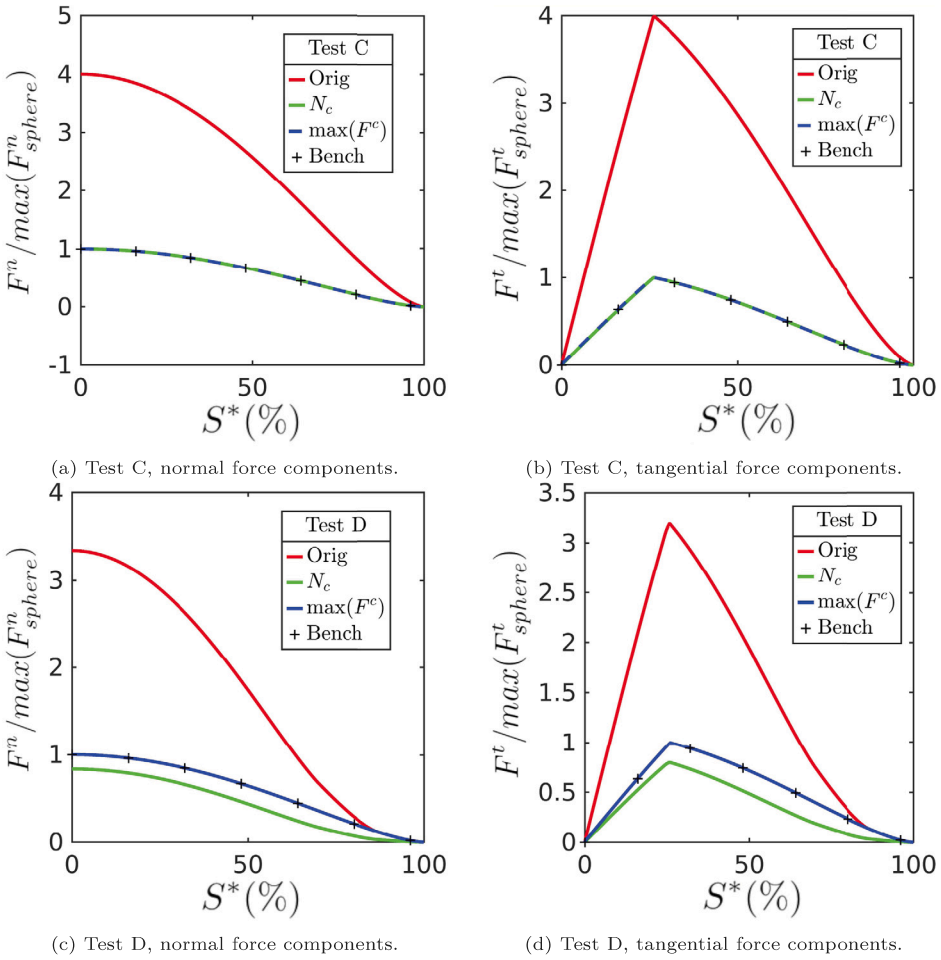

(a) Test C, normal force components.

(b) Test C, tangential force components.

(c) Test D, normal force components.

(d) Test D, tangential force components.

Fig. 18. Normal and tangential force decomposition of Case C and Case D with $N_s = 2$ using the proposed solutions. The forces are normalised against the *maximum* of each force component generated by the appropriate spherical benchmark. The $S^*(\%)$ term is defined as before (see Fig. 11). Orig, represents the unmodified MS-DEM results, with N_c representing the N_c procedure and $max(F^c)$ representing the $max(F^c)$ procedure, with Bench being the spherical benchmark results.

4. Re-run the contact detection and calculate the local effective masses using Eqs. (14) and (17) to (20) and the stored accelerations.
5. Use the local effective masses to calculate the forces acting on the particles and update their kinematics.

The required communication overhead is expected to be small, as a novel point-to-point communication scheme has previously been developed to efficiently handle such problems [8]. Additionally, the required memory overhead is not excessive and scales linearly with the number of MS-DEM particles and not the number of constituent spheres. There is additional computational cost in so far as the contact detection procedure will be run twice. However, for contact detection between spheres, typically the largest computational effort is in the evaluation of neighbour-lists which do not need to be re-evaluated to implement the above scheme. Therefore, it is believed that the local effective mass model will not significantly increase the computational time of a large-scale simulation in comparison to the traditional MS-DEM implementation.

The $max(F^c)$ proposal could be implemented as follows:

1. During the contact detection, store the MS-DEM particle identifiers for pairs of contacting MS-DEM particles and their associated normal and tangential forces.
2. During the contact detection, if multiple contacts are detected by searching the given MS-DEM particle pair list, perform the $max(F^c)$ procedure for the given MS-DEM pair.
3. Before updating particle kinematics, communicate the stored MS-DEM pair information between the relevant processors.
4. Perform a final $max(F^c)$ procedure on the assembled MS-DEM pair information which will generate the final forces required to updated the particle kinematics.

The main difficulty is in the efficient handling of the additional memory overhead. The length of the listed paired particle information would not be expected to exceed 12 pairs (i.e. the maximum possible packing of spherical particles). However, this would become excessive if a shared memory scheme is employed. As such it is recommended that the $max(F^c)$ procedure be implemented using a distributed memory scheme as well as the previously mentioned point-to-point communication scheme [8] to ensure scalability. This is expected to incur a marginal increase in communication and memory overhead in comparison to a traditional MS-DEM implementation.

10.2. Determining the mode of contact

At present it is predicted that three scenarios will be encountered when a user intends to utilise the proposed solutions in this work.

1. The system only contains high-fidelity particles which encounter computational multi-contact points.
2. The system only contains low-fidelity concave particles.
3. The particles in the system are of high fidelity with local concavities.

Table 3
The MS-DEM errors and proposed solutions, see earlier tables for the causes.

Error	Solution
Over-damping in computational multi-contact problem.	$max(F^c)$ procedure.
Over-stiffness in computational multi-contact problem.	$max(F^c)$ procedure.
Over-damping in natural multi-contact problem.	Use a local effective mass.
Under-damping.	Avoid purely velocity based damping.
Contact area topology: Stiffness and damping inconsistencies.	$max(F^c)$ procedure.

The first two scenarios, which must be determined by the user, requires only the application of the proposed implementations of either the $max(F^c)$ procedure or local effective mass model. The more challenging third scenario, will require the development of an automated procedure to determine the mode of contact and utilise the correct procedure. The development of such a scheme is non-trivial and beyond the scope of this paper and will be the subject of future work.

10.3. Consequences for large scale systems

Unexplored in this work is the effect of the identified errors on large scale systems. However, several of the effects of the uncovered errors can be predicted based on previous studies. For example, the effect of over-damping, from a computational or natural multi-contact problem, would be expected to have a non-trivial effect on the macroscopic behaviour of dilute particle systems due to the expected decrease in restitution coefficient [36].

In dense systems, the macroscopic behaviour (in non-dimensional form) is expected to be comparatively unaffected by erroneous over-stiffness and over-damping forces [25]. One would expect, however, that when carrying out microstructural analysis (such as in evaluating the properties of force chains) in dense systems erroneous force calculations would have a non-trivial effect. Additionally, simulations which attempt to model particle attrition naturally depend on accurate force calculations [37], for both dilute and dense systems.

In both dilute and dense systems over-stiffness should be avoided as the required time step size may become prohibitively small to perform large simulations. As such, a major benefit of the $max(F^c)$ procedure is that it produces a contact time commensurate with the spherical benchmarks, i.e. the contact time can be accurately predicted before a simulation can be run and set to match user requirements. This is also true for the case of a natural multi-contact point for which the local effect mass ensures a predictable contact duration. Therefore, it is expected that the implementation of either of the proposed solutions in this work will not have any effects on the stability of a given simulation or require prohibitively small time steps.

11. Conclusion and outlook

11.1. Conclusion

Five types of MS-DEM collision errors have been investigated. Two of these are canonical over-stiffness and over-damping errors occurring at a computational multi-contact point (see Section 1). Three new errors were identified for the first time, these being over-damping in a natural multi-contact problem, under-damping occurring when purely velocity based damping is employed and inconsistent force responses caused by erroneous contact area calculations. The proposed maximum force procedure is shown to remedy the canonical over-stiffness and over-damping errors, along with the erroneous contact area calculations. It was also shown that this force summation procedure is a more general solution to over-stiffness and over-damping than previous proposals in the literature. The concept of a locally reduced mass is demonstrated to mitigate over-damping in a natural multi-contact scenario. Additionally, it is recommended that purely velocity based damping be avoided for use with the MS-DEM to avoid the potential of under-damped behaviour. All errors and associated solutions are provided in Table 3.

An important note worth highlighting is that the locally reduced mass is a property based only on particle dynamics, meaning it is independent of the specific contact model. As such, it's utility should be considered for related contact models in which the reduced mass is used and natural multi-contact problems may arise, such as cohesive/adhesive particle interactions [34,35]. However, the use of a locally reduced mass only solves the issue of over-damping in a natural multi-contact problem, meaning any computational multi-contact problems need to be addressed by other methods, such as the maximum force procedure. As with the locally reduced mass, the $max(F^c)$ procedure should be considered for related contact models used with the MS-DEM. As the calculation of an effective radius (which is a proxy for the contact area) is used in numerous contact models [34,35].

To conclude, if traditional contact models are used with the MS-DEM without modification, there is a high likelihood of large errors being accrued within a simulation. The common foundational source of error is the fundamental force summation procedure used in the MS-DEM, therefore, errors (though not yet specifically identified) will occur for many contact models used with the MS-DEM if unmodified. Similarly, such errors will occur for related methods such as those using polygons and polyhedra [29]. However, the general nature of the proposed solutions in this work will likely be of use for such related methods.

11.2. Outlook

There are additional outstanding problems which must be solved to further improve the accuracy of the MS-DEM. This includes modifications to evaluate forces arising from non-circular contact areas, e.g. faces of two cubes in contact. If this were the case, the $max(F^c)$ procedure would yield incorrect results and it is currently unclear what the most effective strategy should be. As such, further work should be conducted in this area to improve MS-DEM interactions of such scenarios.

Another outstanding issue, as stated in Section 10, is the development of an efficient procedure for distinguishing contact scenarios to apply the most appropriate solutions established in this work.

CRediT authorship contribution statement

Nathan Berry: Conceptualization, Methodology, Software, Validation, Data curation, Writing – original draft. **Yonghao Zhang:** Project administration, Funding acquisition, Writing – review & editing. **Sina Haeri:** Conceptualization, Supervision, Resources, Data curation, Writing – review & editing, Funding acquisition.

Declaration of competing interest

The authors declare that they have no known competing financial interests or personal relationships that could have appeared to influence the work reported in this paper.

Data availability

Data will be made available on request.

Acknowledgements

This work was supported by the UK Engineering and Physical Sciences Research Council (EPSRC) grant EP/T009128/2.

Table A.4
Differential equations constructed for the linear contact models for both the m_e based model and the purely velocity dependant model given by Eqs. (1) and (3) respectively, with the associated α and β terms for the analytical solutions (see Eqs. (A.8) and (A.10). Equations are constructed for classical spherical contacts/collisions and for the test cases A–C. For test cases A and B $m_e' = N_s m_e$.

m_e	Governing equation	α	β
Sphere	$\ddot{\delta} + \gamma_n \dot{\delta} + \frac{K_n}{m_e}\delta = 0$	γ_n	$\sqrt{\frac{K_n}{m_e}}$
Test A	$\ddot{\delta} + N_c\gamma_n \dot{\delta} + \frac{N_c K_n}{m_e'}\delta = 0$	$N_c\gamma_n$	$\sqrt{\frac{N_c K_n}{m_e'}} = \sqrt{\frac{K_n}{m_e}}$
Test B	$\ddot{\delta} + \gamma_n \dot{\delta} + \frac{K_n}{m_e'}\delta = 0$	γ_n	$\sqrt{\frac{K_n}{m_e'}}$
Test C	$\ddot{\delta} + N_c^2\gamma_n \dot{\delta} + \frac{N_c^2 K_n}{m_e}\delta = 0$	$N_c^2\gamma_n$	$\sqrt{\frac{N_c^2 K_n}{m_e}}$
Vel.	Governing equation	α	β
Sphere	$\ddot{\delta} + \frac{\gamma_n}{m_e}\dot{\delta} + \frac{K_n}{m_e}\delta = 0$	$\frac{\gamma_n}{m_e}$	$\sqrt{\frac{K_n}{m_e}}$
Test A	$\ddot{\delta} + \frac{N_c\gamma_n}{m_e'}\dot{\delta} + \frac{N_c K_n}{m_e'}\delta = 0$	$\frac{N_c\gamma_n}{m_e'} = \frac{\gamma_n}{m_e}$	$\sqrt{\frac{K_n}{m_e}} = \sqrt{\frac{K_n}{m_e}}$
Test B	$\ddot{\delta} + \frac{\gamma_n}{m_e'}\dot{\delta} + \frac{K_n}{m_e'}\delta = 0$	$\frac{\gamma_n}{m_e'}$	$\sqrt{\frac{K_n}{m_e'}}$
Test C	$\ddot{\delta} + \frac{N_c^2\gamma_n}{m_e}\dot{\delta} + \frac{N_c^2 K_n}{m_e}\delta = 0$	$\frac{N_c^2\gamma_n}{m_e}$	$\sqrt{\frac{N_c^2 K_n}{m_e}}$

Appendix A. Analytical solutions

For the test cases A–C, linear second-order homogeneous differential equations can be constructed to describe the particle systems (see Table A.4). All of these equations are amenable to the same analysis process, for which Eq. (A.1) is used to derive general solutions for the duration of contact, velocity response and coefficient of restitution. Note, the following equations are formed for the quasi-one dimensional test cases and are written in scalar form, which is to be assumed for the remainder of the work. Additionally, subscripts i, j or AB will be dropped, unless additional distinction is needed in which case the meanings will be clear. The general form of governing equation is given by

$$\ddot{\delta} + \alpha\dot{\delta} + \beta^2\delta = 0, \tag{A.1}$$

where δ is the inter-particle overlap (see Fig. 7) with $\dot{\delta}$ (relative velocity) and $\ddot{\delta}$ (relative acceleration) the first and second derivatives with the respect to time t. The α and β terms are then specific to the contact model and test case, given in Table A.4, which can simply be substituted into the general solutions given below.

The roots of the characteristic equation of Eq. (A.1), can then be given with $r = -\varepsilon\beta \pm \beta\sqrt{\varepsilon^2 - 1}$ where

$$\varepsilon = \frac{\alpha}{2\beta}, \tag{A.2}$$

is the system damping factor. Assuming an underdamped system, $\varepsilon < 1$, then the roots of the characteristic equation can be written as $r = -\varepsilon\beta \pm i\omega_d$ for which

$$\omega_d = \beta\sqrt{1 - \varepsilon^2}, \tag{A.3}$$

is the damped natural frequency.

The general solution of a linear homogeneous second-order differential equation with complex conjugate roots can be written as

$$\delta = X\exp(-\varepsilon\beta t)\sin(\omega_d t + \phi) \tag{A.4}$$

where X is the amplitude of displacement and ϕ is the phase angle [38], which are given by

$$X = \sqrt{\delta_o^2 + \left(\frac{\dot{\delta_o}^2 + \varepsilon\beta\delta_o}{\omega_d}\right)^2}, \tag{A.5}$$

$$\phi = \tan^{-1}\left(\frac{\omega_d\delta_o}{\dot{\delta}_o + \varepsilon\beta\delta_o}\right), \tag{A.6}$$

where δ_o and $\dot{\delta}_o$ are the initial overlap and the initial relative particle velocity respectively. With the initial condition $\delta_o = 0$, Eq. (A.4) can be written as

$$\delta = \frac{\dot{\delta}_o}{\omega_d}\exp(-\varepsilon\beta t)\sin(\omega_d t), \tag{A.7}$$

then taking the derivative with respect to t, we get

$$\dot{\delta} = \dot{\delta}_o\exp(-\varepsilon\beta t)\cos(\omega_d t) - \frac{\varepsilon\beta\dot{\delta}_o}{\omega_d}\exp(-\varepsilon\beta t)\sin(\omega_d t). \tag{A.8}$$

From the above equations, by applying appropriate conditions, one can deduce the contact time t_c and the coefficient of restitution e. At the end of a contact duration, there is no particle overlap by definition, i.e. $\delta(t_c) = 0$. Therefore, from Eq. (A.7), it is clear that the contact time is given by

$$t_c = \pi/\omega_d. \tag{A.9}$$

For the coefficient of restitution, the following definition can be used:

$$e = \left|\frac{\dot{\delta}'}{\dot{\delta}}\right| = \left|\frac{\dot{\delta}(t_c)}{\dot{\delta}_o}\right| = \exp\left(-\frac{\varepsilon\pi}{\sqrt{1-\varepsilon^2}}\right) \tag{A.10}$$

with $\dot{\delta}(t_c)$ determined from Eq. (A.8).

A.1. Force deconstruction boundary conditions

Due to the change in boundary conditions proposed in Section 5.4, Eqs. (A.5) to (A.8) need to be modified by substituting boundary conditions, $\delta_o > 0$ and $\dot{\delta}_o = 0$, resulting in the new contact duration:

$$t_c = \frac{\pi + \phi}{\omega_d}. \tag{A.11}$$

A.2. Contact area differences

Derivation of effective radius R_e, relationships for the test cases C and D with $N_s = 2$. The definition of the effective radius, as given earlier, is $R_e = (r_i r_j)/(r_i + r_j)$. Using the MS-DEM force procedure, Eq. (9), the total effective contact area in an MS-DEM interaction can be quantified with $\sqrt{R_{e,AB}} = \sum_{c=1}^{N_c}\sqrt{R_{e,c}}$, where $R_{e,AB}$ is the total computed effective radius of the MS-DEM particles and $R_{e,c}$ is the effective radius of a specific contact. Using the definition of R_e, the effective radius for the spherical benchmark would be $R_{e,sphere} = r_{sphere}/2$ with the radii of the spherical benchmark being r_{sphere}. For the test case C, each contact is between spheres with identical radii

to the benchmark case. With the test case C and $N_s = 2$, there are $N_c = 4$ contacts. As such the resulting effective contact area is given by $\sqrt{R_{e,AB}} = \sum_{c=1}^{N_c} \sqrt{R_{e,c}} = 4\sqrt{r_{sphere}/2} = 2\sqrt{2}\sqrt{r_{sphere}}$.

For the test case D, the situation is slightly more complex. The smaller embedded constituent sphere has a radius $r_s = r_{sphere}/2$ with the larger sphere having radius $r_l = r_{sphere}$. As with the test case C four contacts are present, one contact appears for the larger sphere interactions, and the effective radii of this interaction is demarcated with $R_{e,ll} = r_{sphere}/2$. Another interaction is between the two smaller spheres, with the effective radius of this interaction given with $R_{e,ss} = r_{sphere}/4$. The final two interactions are between a small sphere and a large sphere, with the effective radius demarcated with $R_{e,ls} = r_{sphere}/3$. Therefore, the total effective radius for the MS-DEM particles in the test case D is given by

$$\sqrt{R_{e,AB}} = \sum_{c=1}^{N_c} \sqrt{R_{e,c}}, \tag{A.12}$$

$$\sqrt{R_{e,AB}} = \sqrt{R_{e,ll}} + \sqrt{R_{e,ss}} + 2\sqrt{R_{e,ls}}, \tag{A.13}$$

$$\sqrt{R_{e,AB}} = \sqrt{r_{sphere}/2} + \sqrt{r_{sphere}/4} + 2\sqrt{r_{sphere}/3} = 2.36\sqrt{r_{sphere}}. \tag{A.14}$$

Appendix B. Additional results

See Figs. B.19–B.27.

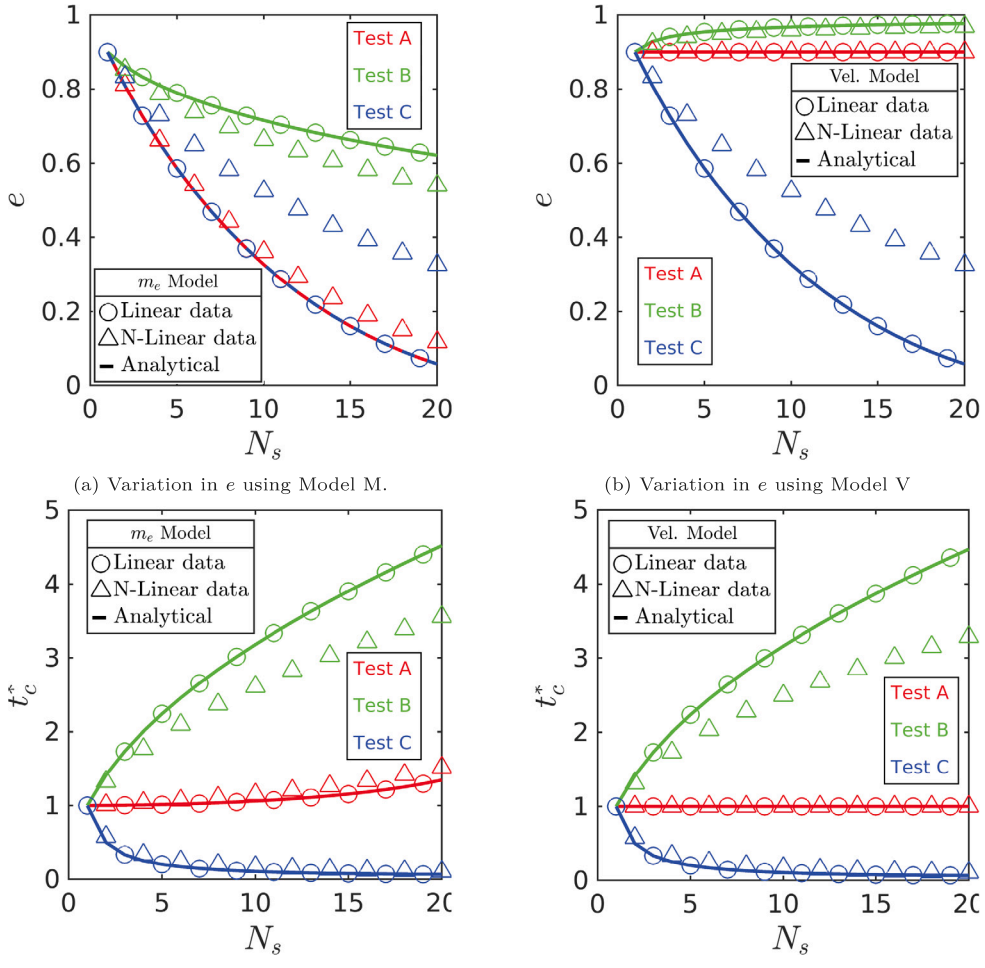

(a) Variation in e using Model M.

(b) Variation in e using Model V

(c) Variation in t_c^* using Model M.

(d) Variation in t_c^* using Model V.

Fig. B.19. Analytical predictions for changes in e and t_c^* with respect to N_s for Model M and Model V and all test cases. Symbols represent simulation data and solid lines are the analytical predictions (linear models). In the legends, m_e Model corresponds to Model M data, with Vel. Model corresponding to Model V.

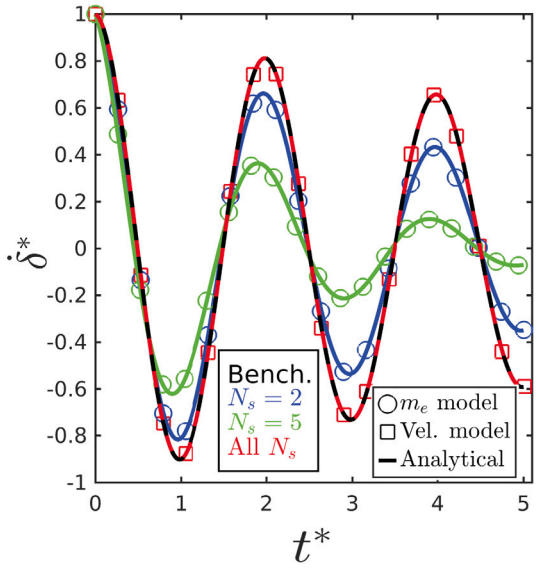

Fig. B.20. Test A's velocity responses. All results are analytical predictions using Model M and Model V. The parameters $\dot{\delta}^*$ and t_c^* are defined as given in Section 5.3. In the legends, m_e model corresponds to Model M data, with Vel. model corresponding to Model V and Bench being the spherical benchmark results.

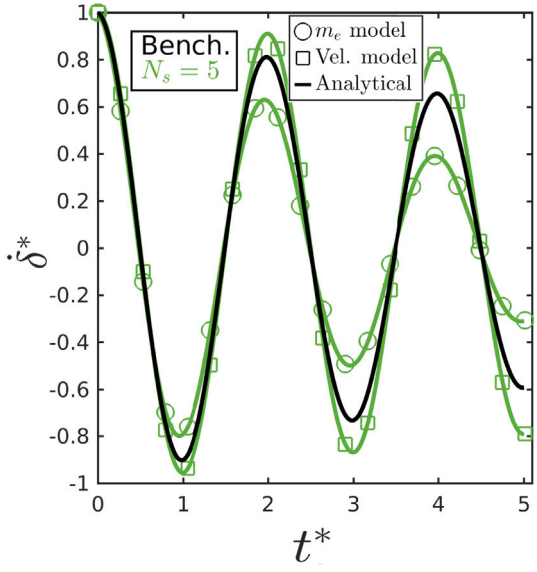

Fig. B.21. Test B's velocity responses. All results are analytical predictions using Model M and Model V. The parameters $\dot{\delta}^*$ and t_c^* are defined as given in Section 5.3. In the legends, m_e model corresponds to Model M data, with Vel. model corresponding to Model V and Bench being the spherical benchmark results.

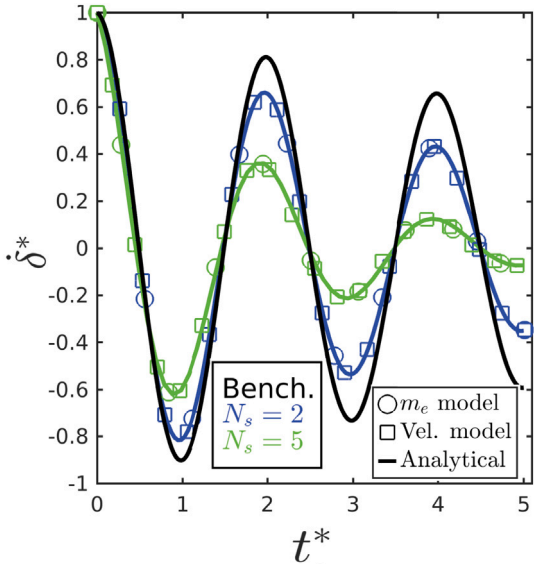

Fig. B.22. Test C's velocity responses. All results are analytical predictions using Model M and Model V. The parameters $\dot{\delta}^*$ and t_c^* are defined as given in Section 5.3. In the legends, m_e model corresponds to Model M data, with Vel. model corresponding to Model V and Bench being the spherical benchmark results.

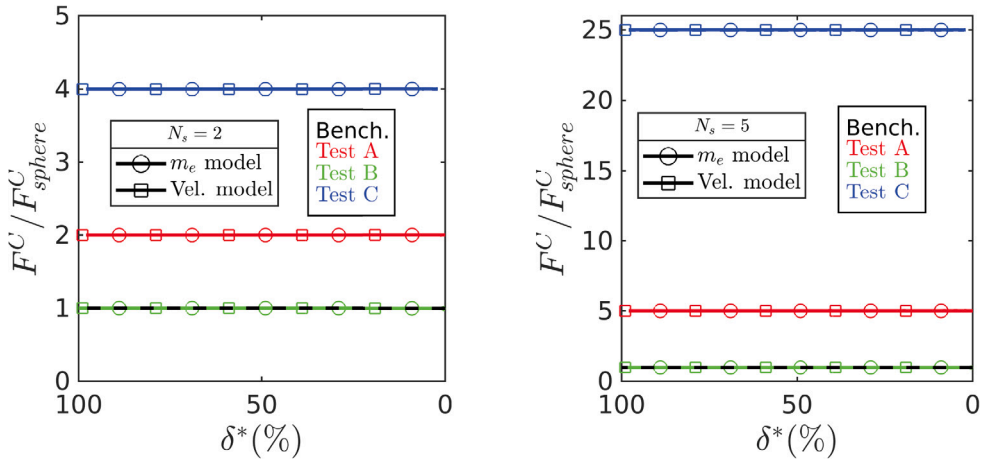

(a) Conservative force responses with $N_s = 2$. (b) Conservative force responses with $N_s = 5$.

Fig. B.23. Analytical conservative force decomposition of Model M and Model V with the original test cases A–C. All parameters, F^C and F^C_{sphere} and δ^*, are defined identically as given in Section 5.4. Bench represents the spherical benchmark results. In the legends, m_e model corresponds to Model M data, with Vel. model corresponding to Model V .

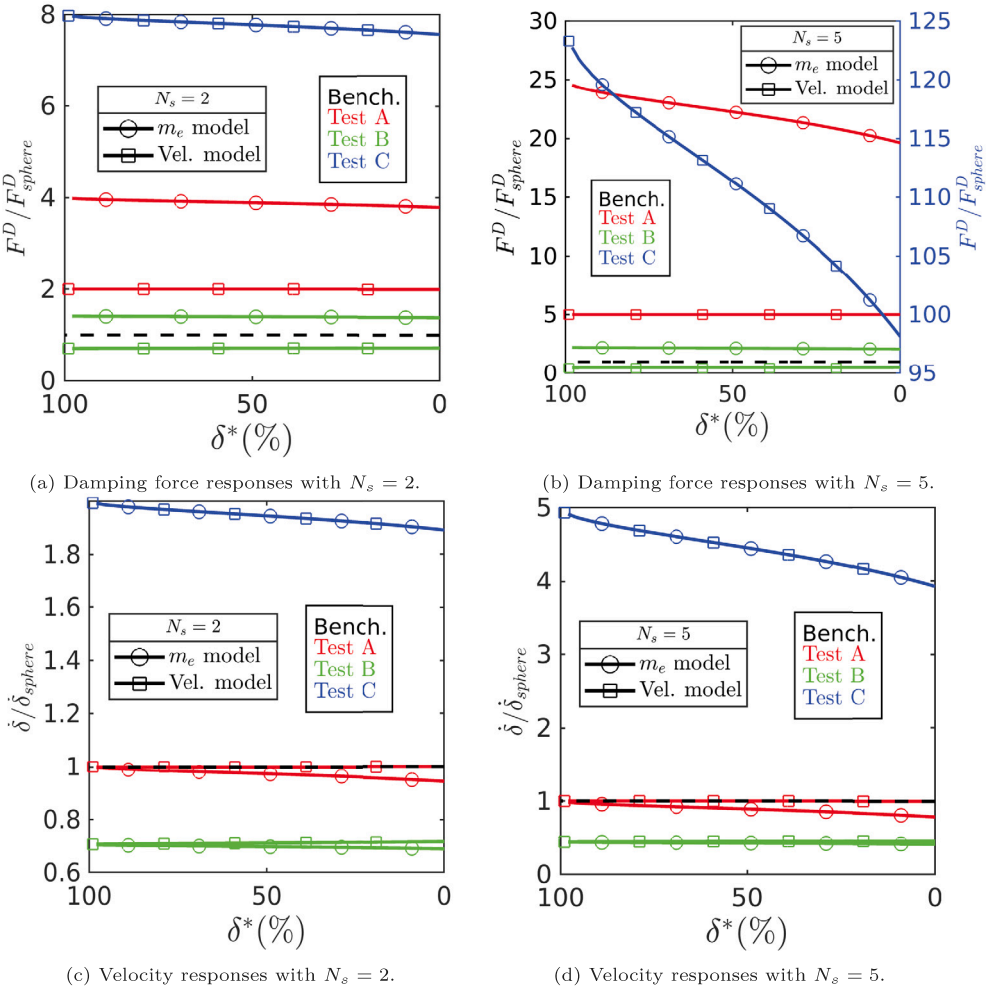

(a) Damping force responses with $N_s = 2$. (b) Damping force responses with $N_s = 5$.

(c) Velocity responses with $N_s = 2$. (d) Velocity responses with $N_s = 5$.

Fig. B.24. Analytical damping force decomposition and velocity response of Model M and Model V with the original test cases A–C. All parameters, F^D, F^D_{sphere}, $\dot{\delta}$, $\dot{\delta}_{sphere}$ and δ^*, are defined identically as given in Section 5.4. Bench represents the spherical benchmark results. In the legends, m_e model corresponds to Model M data, with Vel. model corresponding to Model V.

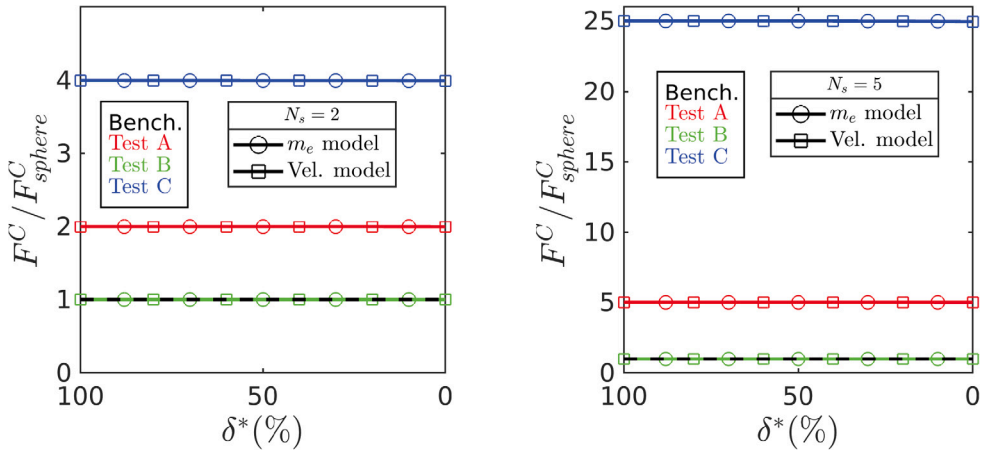

(a) Conservative force responses with $N_s = 2$.

(b) Conservative force responses with $N_s = 5$.

Fig. B.25. Conservative force decomposition of Model NLM and Model NLV with the original test cases A–C. All parameters, F^C and F^C_{sphere} and δ^*, are defined identically as given in Section 5.4. All results are taken from simulation data. Bench represents the spherical benchmark results. In the legends, m_e model corresponds to Model NLM data, with Vel. model corresponding to Model NLV.

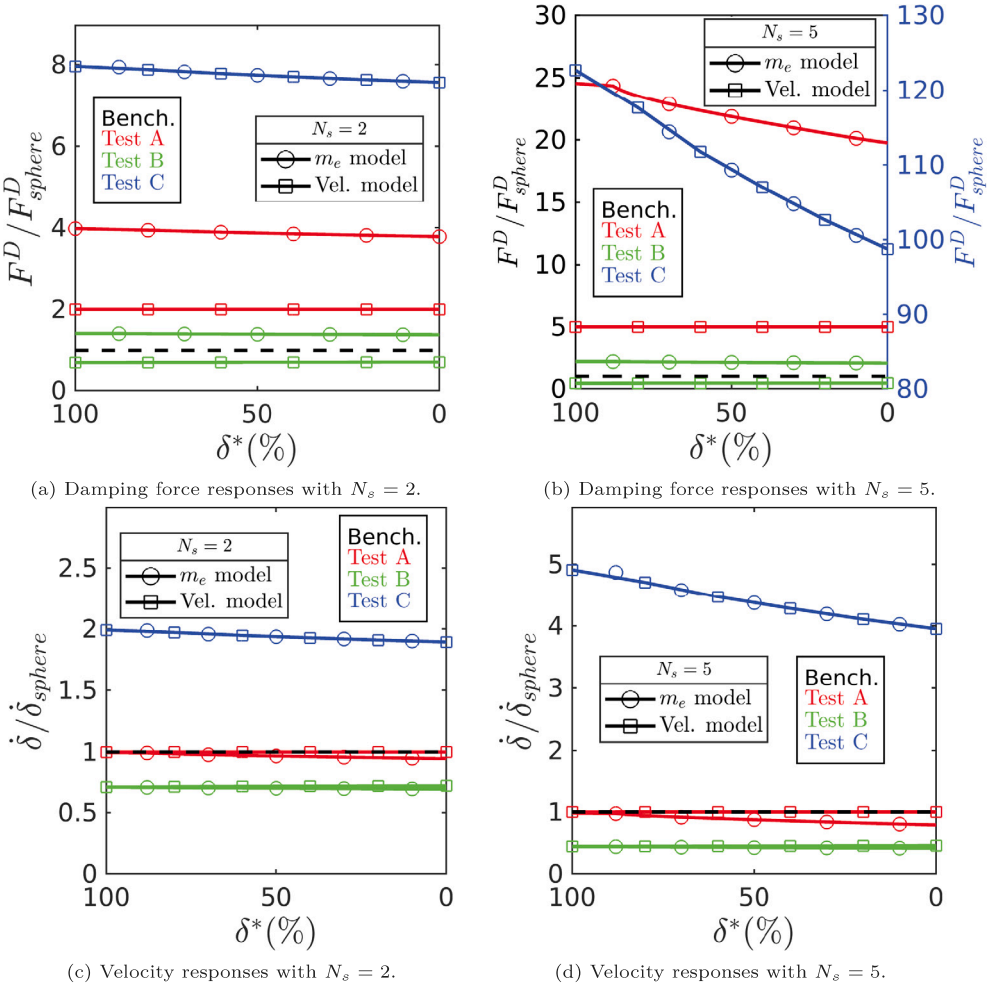

(a) Damping force responses with $N_s = 2$.

(b) Damping force responses with $N_s = 5$.

(c) Velocity responses with $N_s = 2$.

(d) Velocity responses with $N_s = 5$.

Fig. B.26. Damping force decomposition and velocity response of Model NLM and Model NLV with the original test cases A–C. All parameters, F^D, F^D_{sphere}, $\dot{\delta}$, $\dot{\delta}_{sphere}$ and δ^*, are defined identically as given in Section 5.4. All results are taken from simulation data. Bench represents the spherical benchmark results. In the legends, m_e model corresponds to Model NLM data, with Vel. model corresponding to Model NLV.

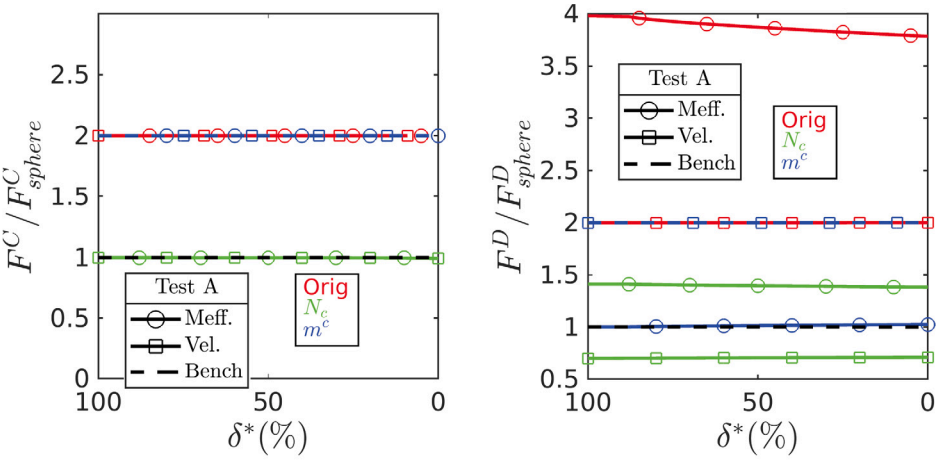

(a) Test A, conservative forces.

(b) Test A, damping forces.

(c) Test C, conservative forces.

(d) Test C, damping forces.

Fig. B.27. Conservative and damping force decomposition of Model NLM and Model NLV with the proposed MS-DEM solutions for test cases A and C. All parameters, F^C, F^C_{sphere}, F^D, F^D_{sphere} and δ^*, are defined identically as given in Section 5.4. Orig, represents the unmodified MS-DEM results, with N_c representing the N_c procedure and m^c representing the use of a locally reduced mass, with Bench being the spherical benchmark results. All results are extracted from simulations. In the legends, Meff corresponds to Model NLM data, including the locally reduced mass, with Vel. corresponding to Model NLV.

References

[1] K. Ridgway, R. Rupp, The effect of particle shape on powder properties, J. Pharm. Pharmacol. 21 (1969) 30S–39S.

[2] T. Horio, M. Yasuda, S. Matsusaka, Effect of particle shape on powder flowability of microcrystalline cellulose as determined using the vibration shear tube method, Int. J. Pharm. 473 (2014) 572–578.

[3] M. Alizadeh, A. Hassanpour, M. Pasha, M. Ghadiri, A. Bayly, The effect of particle shape on predicted segregation in binary powder mixtures, Powder Technol. 319 (2017) 313–322.

[4] S. Haeri, Y. Wang, O. Ghita, J. Sun, Discrete element simulation and experimental study of powder spreading process in additive manufacturing, Powder Technol. 306 (2017) 45–54.

[5] S. Haeri, Optimisation of blade type spreaders for powder bed preparation in additive manufacturing using dem simulations, Powder Technol. 321 (2017) 94–104.

[6] R. Escudie, N. Epstein, J.R. Grace, H.T. Bi, Effect of particle shape on liquid-fluidized beds of binary (and ternary) solids mixtures: segregation vs. mixing, Chem. Eng. Sci. 61 (2006) 1528–1539.

[7] G. Karthik, V.V. Buwa, Effect of particle shape on catalyst deactivation using particle-resolved cfd simulations, Chem. Eng. J. 377 (2019) 120164.

[8] T.D. Nguyen, S.J. Plimpton, Aspherical particle models for molecular dynamics simulation, Comput. Phys. Comm. 243 (2019) 12–24.

[9] G. Lu, J. Third, C. Müller, Discrete element models for non-spherical particle systems: From theoretical developments to applications, Chem. Eng. Sci. 127 (2015) 425–465.

[10] W. Zhong, A. Yu, X. Liu, Z. Tong, H. Zhang, Dem/cfd-dem modelling of non-spherical particulate systems: theoretical developments and applications, Powder Technol. 302 (2016) 108–152.

[11] P.A. Cundall, O.D. Strack, A discrete numerical model for granular assemblies, Geotechnique 29 (1979) 47–65.

[12] J. Favier, M. Fard, M. Kremmer, A. Raji, Shape representation of axi-symmetrical, non-spherical particles in discrete element simulation using multi-element model particles, Eng. Comput. 16 (1999) 467–480.

[13] K.M. Salerno, D.S. Bolintineanu, G.S. Grest, J.B. Lechman, S.J. Plimpton, I. Srivastava, L.E. Silbert, Effect of shape and friction on the packing and flow of granular materials, Phys. Rev. E 98 (2018) 050901.

[14] P. Langston, A.R. Kennedy, H. Constantin, Discrete element modelling of flexible fibre packing, Comput. Mater. Sci. 96 (2015) 108–116.

[15] A. Podlozhnyuk, S. Pirker, C. Kloss, Efficient implementation of superquadric particles in discrete element method within an open-source framework, Comput. Part. Mech. 4 (2017) 101–118.

[16] A. Di Renzo, F.P. Di Maio, Comparison of contact-force models for the simulation of collisions in dem-based granular flow codes, Chem. Eng. Sci. 59 (2004) 525–541.

[17] S. Luding, Cohesive, frictional powders: contact models for tension, Granul. Matter 10 (2008) 235–246.

[18] J. Horabik, M. Molenda, Parameters and contact models for dem simulations of agricultural granular materials: A review, Biosyst. Eng. 147 (2016) 206–225.

[19] M.H. Abbaspour-Fard, Theoretical validation of a multi-sphere, discrete element model suitable for biomaterials handling simulation, Biosyst. Eng. 88 (2004) 153–161.

[20] H. Kruggel-Emden, S. Rickelt, S. Wirtz, V. Scherer, A study on the validity of the multi-sphere discrete element method, Powder Technol. 188 (2008) 153–165.

[21] M. Price, V. Murariu, G. Morrison, Sphere clump generation and trajectory comparison for real particles, Proc. Discret. Elementoorg. Model. 2007 (2007).

[22] M. Kodam, R. Bharadwaj, J. Curtis, B. Hancock, C. Wassgren, Force model considerations for glued-sphere discrete element method simulations, Chem. Eng. Sci. 64 (2009) 3466–3475.

[23] D. Höhner, S. Wirtz, H. Kruggel-Emden, V. Scherer, Comparison of the multi-sphere and polyhedral approach to simulate non-spherical particles within the discrete element method: Influence on temporal force evolution for multiple contacts, Powder Technol. 208 (2011) 643–656.

[24] J.K. Chow, P. Tai, J. Li, Z. Li, W. Wang, Over-stiff and over-damped problem of multi-sphere approach for ellipse-wall collision using discrete element method, Powder Technol. 394 (2021) 735–747.

[25] L.E. Silbert, D. Ertaş, G.S. Grest, T.C. Halsey, D. Levine, S.J. Plimpton, Granular flow down an inclined plane: Bagnold scaling and rheology, Phys. Rev. E 64 (2001) 051302.

[26] N.V. Brilliantov, F. Spahn, J.-M. Hertzsch, T. Pöschel, Model for collisions in granular gases, Phys. Rev. E 53 (1996) 5382.

[27] H. Zhang, H. Makse, Jamming transition in emulsions and granular materials, Phys. Rev. E 72 (2005) 011301.

[28] N. Berry, Y. Zhang, S. Haeri, Lees–Edwards boundary conditions for the multi-sphere discrete element method, Powder Technol. 389 (2021) 292–308.

[29] A.G. Neto, P. Wriggers, Discrete element model for general polyhedra, Comput. Part. Mech. 9 (2022) 353–380.

[30] A.D. Rakotonirina, J.-Y. Delenne, F. Radjai, A. Wachs, Grains3d, a flexible dem approach for particles of arbitrary convex shape–part iii: extension to non-convex particles modelled as glued convex particles, Comput. Part. Mech. 6 (2019) 55–84.

[31] W. Goldsmith, Impact: The Theory and Physical Behavior of Colliding Solids, E. Arnold, 1960.

[32] A. Aryaei, K. Hashemnia, K. Jafarpur, Experimental and numerical study of ball size effect on restitution coefficient in low velocity impacts, Int. J. Impact Eng. 37 (2010) 1037–1044.

[33] C. Thornton, Coefficient of restitution for collinear collisions of elastic-perfectly plastic spheres, J. Appl. Mech. 64 (1997) 383–386.

[34] A.P. Thompson, H.M. Aktulga, R. Berger, D.S. Bolintineanu, W.M. Brown, P.S. Crozier, P.J. in 't Veld, A. Kohlmeyer, S.G. Moore, T.D. Nguyen, R. Shan, M.J. Stevens, J. Tranchida, C. Trott, S.J. Plimpton, Lammps - a flexible simulation tool for particle-based materials modeling at the atomic, meso, and continuum scales, Comput. Phys. Comm. 271 (2022) 108171.

[35] J. Wittenburg, Dynamics of Multibody Systems, second ed., Springer-Verlag, 2008.

[36] S. Chialvo, S. Sundaresan, A modified kinetic theory for frictional granular flows in dense and dilute regimes, Phys. Fluids 25 (2013) 070603.

[37] T. Brosh, H. Kalman, A. Levy, Dem simulation of particle attrition in dilute-phase pneumatic conveying, Granul. Matter 13 (2011) 175–181.

[38] A.A. Shabana, Theory of Vibration: An Introduction, Springer, 2018.